Defence Science Journal, Vol. 53. No. 3, July 2003, pp. 281-324
© 2003, DESIDOC

REVIEW PAPER

Mercury Cadmium Telluride Photoconductive Long Wave Infrared Linear Array Detectors

Risal Singh and Vandna Mittal

Solid State Physics Laboratory, Delhi – 110 054

ABSTRACT

Mercury cadmium telluride ($Hg_{1-x}Cd_xTe$) (MCT) photoconductive long wave infrared linear arrays are still in demand due to several advantages. The linear array technology is well established, easier, economical and is quite relevant to thermal imaging even today. The scan thermal imaging systems based on this technology offer wider field of view coverage and capacity for higher resolution in the scan direction relative to staring systems that use expensive and yet to mature focal plane array detector technology. A critical review on photoconductive n-$Hg_{1-x}Cd_xTe$ linear array detector technology for the long wave infrared range has been presented. The emphasis lies on detector design and processing technology. The critical issues of diffusion and drift effects, Hi-Lo and heterostructure blocking contacts, surface passivation, and other related aspects have been considered from the detector design angle. The device processing technology aspects are of vital importance.

Keywords: Photoconductor, infrared detector, LWIR, linear array, processing, passivation, overlap, design, blocking contacts, heterostructure, responsivity, noise, detectivity

NOMENCLATURE

λ	Wavelength
ω	Modulation frequency
α	Absorption coefficient
α_1	Diffusion length along the direction of electric field
α_2	Diffusion length against the direction of electric field
η	Quantum efficiency
η_0	Internal quantum efficiency
θ	Angular view of the background
ϕ	Signal photon flux
μ	Ambipolar drift mobility
μ_a	Ambipolar mobility
μ_e	Mobility of majority carriers
μ_h	Mobility of minority carriers
μ_s	Surface electrons mobility
τ_{bulk}	Bulk lifetime
τ	Excess carrier lifetime/recombination time
τ_a	Sweep-out lifetime
τ_{Ai1}	Intrinsic Auger 1 lifetime
τ_{ef}	Effective lifetime considering sweep-out effect
τ_{eff}	Effective lifetime
τ_p	Minority carrier lifetime

Revised 13 March 2003

τ_{pixel} Dwell time

τ_{net} Effective lifetime taking into account surface recombination

λ_c Cutoff wavelength

λ_p Peak response wavelength

A Detector active area lw

b Ratio of μ_e to μ_h

d Detector thickness

D Ambipolar diffusion coefficient

D^* Normalised detectivity

D^*_λ Normalised spectral detectivity

D^*_{hf} Detectivity at high frequency

D^*_{BLIP} Detectivity of background-limited infrared photodetector

D_p Minority carrier diffusion coefficient

D_{it} Interface trap density

ΔE Energy barrier

E Bias electric field

f Modulation frequency

f_{g-r} *g-r* cutoff frequency

$f\#$ FOV

f_c Corner frequency

Δf Bandwidth in Hertz

g Photoconductive gain

g_b Background generation rate per unit volume

g_{th} Thermal generation rate per unit volume

G Number of ions striking the MCT per second

I_{beam} Ion milling beam current

k Boltzmann constant

l Detector length

$l_{1,2}$ Length of heavily doped end regions in blocking contacts

L Distance between electrical contacts in overlap structure

L' Length of the detector in SPRITE

L_p Minority carrier diffusion length

n_0 Thermal equilibrium concentration of electrons

n_i Intrinsic carrier concentration

n_s Density of surface electrons in the accumulation layer

N_a Concentration of mercury vacancies initially present

p_0 Thermal equilibrium concentration of holes

p_b Optically generated background hole density

Δp Excess minority carrier density

P_λ Incident power

P_{BB} blackbody radiant power falling on detector at a temperature T

Q_b Background flux

Q_B^o 300 K background irradiance

Q_f Fixed-charge density

r_1 Reflection coefficient from front surface

r_2 Reflection coefficient from back surface

R_λ Voltage spectral responsivity

R_v Voltage responsivity

R_{BB} Blackbody voltage responsivity

R' Detector resistance per unit length

R_c Contact resistance

R_D Detector resistance

R_dC_d Depletion region time constant

R_L Series load resistor

s Pixel rate

S_{srv} Surface recombination velocity

t_d Transit time of electron across the detector

t_{etch} Ion beam milling time

T Absolute temperature in K

$v_d\tau$ Drift length

v_s Velocity at which the target image scans the strip

V Volume of converted material during milling

$V_{1/f}$ $1/f$ noise

V_a Preamplifier noise

V_b Bias voltage

V_{g-r} g-r noise

V_j Johnson noise

V_n Total noise voltage

V_s Photo signal

w Detector width

ΔW Signal power

W Element width (SPRITE)

1. INTRODUCTION

1.1 Thermal Imaging

A tremendous effort has been made on developing the capability to see during conditions of darkness and obscured visibility. The motivation is to extend all daylight activities to periods of darkness, especially for activities involving safety and defence[1,2]. This is possible through natural/artificial illumination or infrared (IR) thermal imaging. The approach involving amplification of small amount of natural illumination employs image intensifiers and requires lighting equivalent to a bright starlit night and clear weather conditions free from clouds, fog, smoke, or thick dust. The technique of artificial illumination, though very versatile, suffers from several shortcomings, such as being ineffective in conditions of obscurity created by fog, smoke, and dust. Also being of active nature, this method of imaging betrays the secrecy of presence and location of the observer being detected by the enemy in security and military environment.

An IR thermal imaging system does not suffer from the above limitations and can detect the electromagnetic radiation emitted by all objects. The blackbody or thermal emission described by the Planck's law is a function of the body's temperature and emissivity. The intensity of radiation and its peak frequency increases with temperature. The sun at 6000 K has a peak at emission wavelength near 500 nm lying in the middle of visible spectrum. The terrestrial objects at 300 K have peak in the IR region at ~ 10 µm in the 8-14 µm atmospheric window. An IR imaging system also works in 3-5 µm atmospheric window by detecting radiation emitted in the tail of the Planck curve, or by detecting reflected IR sunlight during daytime operation. Since the wavelength of the detected IR radiation is many times that of the visible light, this radiation is scattered much less by water vapour or particulates. Consequently, IR thermal imaging[3-20] can provide superior performance under conditions of fog, clouds, smoke, and dust. Essentially, a thermal image is a two-dimensional mapping of the change in the IR radiance of a scene as a function of angular coordinates. The radiance being imaged is the sum of the object's graybody emission plus any energy reflected from the object. The atmosphere between the source and sensor attenuates this total radiance. The wavebands of principal interest for thermal imaging are mid-wavelength infrared (MWIR) (3µm to 5µm) and long wavelength infrared (LWIR) (8µm to 12 µm) bands. The useful infrared energy available at the sensor depends upon the temperature and emittance of the source, the spectral bandwidth to which the sensor responds and the atmospheric transmittance of the path[21].

1.2 Scanning versus Staring

With the development of photovoltaic 2-D focal plane arrays (FPAs), there has been a shift in the technology focus from photoconductive linear arrays to FPAs. In a staring system, the entire field of view is imaged onto an array of infrared detectors. Video signal processing, including pre-amplification and multiplexing, is usually required to read the video data of the array. The 2-D FPAs offer advantages like being staring-type, the complex opto-mechanical scanning is avoided, higher output impedance helps in interfacing, compatibility with readout integrated circuits (ROICs) and low power dissipation. Also, as the staring systems are able to integrate the incident energy over a relatively longer time interval, they exhibit the lowest noise equivalent temperature difference (NETD) (typically < 0.1 K). However, the staring arrays offer limited field of view (FOV) and suffer from image under-sampling[6,21]. The FPA technology is still emerging and has a long way to

mature. Only limited production of the FPAs has been undertaken the world over because of the low yield (high cost) and other technological difficulties. In satellite surveillance and in other imaging applications, the FPA's staring concept holds good for sensors placed in geosynchronous orbit where line of sight is stabilised to a point on earth. As the sensor and the earth move insynchrony, the image on FPA remains fixed and the moving targets wrt each can be detected. However, even small motions induced by drift or jitter of sensor and/or spacecraft cause limitation of this concept, leading to clutter-induced noise. Also, the range and resolution dictate the use of extremely large optical systems with FPA elements greater than 10^8.

In a scanned system, opto-mechanical scanning of detector element (or elements) is often used in IR systems to cover 2-D FOV with fewer detectors than would be required to cover whole FOV simultaneously as in a staring system. The scanning systems [which employ both the photoconductive as well as linear FPA] can be designed to cover large over-sampled FOVs, but reduced integration time[21] (dwell time) can raise NETD to 0.2 K or 0.3 K. The scanned systems with photoconductive IR linear arrays are still in demand due to several advantages. The photoconductive linear array technology is well established and the routine large volume production of relatively high yield (low cost) arrays by several manufacturers continues. The linear arrays are relatively easier to scale up in size.

Two fundamental issues for any detector system are sensitivity and resolution. The staring system offers improved sensitivity due to its longer integration/dwell time and can collect photo generated signal for as much as a frame time, in contrast to a scanner system where detectors are to be shared with multiple points in the image space, lowering the dwell time. On the other hand, the requirement of the sampling frequency (twice that of the sensor cutoff frequency) can be fulfilled easily in a scanner system providing better resolution in scan direction. This is not possible in a staring system and affects resolution. This shortcoming, though may be circumvented using micro scanning, but it adds to system complexity. A summary[20] of comparative merits of the two systems is given in Table 1.

Table 1. Comparison of scanning versus staring sensor

Scanning sensor	Staring sensor
Wide field of view	FOV limited to array size
Lower sensitivity due to shorter dwell time	Higher sensitivity due to longer dwell time
Optics to accommodate scanner	Simple optical design
Scanner increases size and reduces reliability	No moving part, more reliable
Requires line-to-line equalisation	Requires individual detector non uniformity correction
High resolution in scan direction	Relatively lower resolution
Well matured and simpler detector fabrication technology	Yet to mature and very difficult detector fabrication technology
Easier to scale up the array size	Difficult to scale up the array size

1.3 Perspective of IR Detectors

The two principal types of semiconductor IR detectors are photon and thermal detectors, depending on the nature of photon interaction with material[22-27]. In the first category, the photon absorption causes generation of electron-hole pairs. The change in electrical energy distribution resulting from this absorption gives rise to an observable electrical signal. These photon detectors can be further divided into four subgroups: (i) intrinsic direct band gap like MCT, (ii) extrinsic type like *Si*(*In*, *Ge*) and *Ge* (*Cu*, *Hg*), (iii) photoemissive-type such as metal silicides and negative electron affinity materials, and (iv) quantum wells (III-V and II-VI ternary and quaternary compounds). The photoconductive and photovoltaic phenomena are the two widely exploited modes of photon detectors. The photon detectors are highly sensitive to radiation and operate in a particular bandwidth only. The thermal detectors fall in the other category where the radiation absorption, either directly in the material or by the auxiliary black surface coating, leads to change in some temperature-dependent properties such as electrical resistance for thermistor bolometer and the internal polarisation for the pyroelectric detectors, and so

on. The thermal detectors are generally wavelength-independent.

The IR detectors are passive devices and have gained much use in defence and security in the last five decades. For such applications, high performance and fast response are the essential requirements. High performance is obtained by cooling the detectors to low temperatures, which also raises their cost. However, the improved performance of cooled detectors justifies their higher unit cost. A high sensitivity and fast response detection of IR radiation is achieved using the semiconductor photon detectors. At present, $Hg_{1-x}Cd_xTe$ is one of the most widely used tunable bandgap semiconductor for IR photon detectors[26], both from fundamental considerations and the material flexibility. The specific advantages of $Hg_{1-x}Cd_xTe$ are the direct energy gap, ability to obtain both low and high carrier concentrations, high mobility of electrons, and comparatively low dielectric constant. In the case of direct narrow gap semiconductors, the optical absorption is much higher than in the extrinsic detectors.

Historically, the photoconductive effect was discovered in selenium[28] by Smith in 1873. The very first IR detectors fabricated, using naturally occurring *PbS* or galena and other materials, were reported by Bose[29] in 1904 in a US patent, in which he had described the detectors in almost all wavelength ranges, including IR. The first Tl_2S IR photoconductor of high responsivity was developed by Case[30]. The initial work on improved photoconductive detectors was done mainly in Germany[31,32] using *PbS*. The production of *PbS* detectors was mostly done in USA and UK[33] and these detectors were used in World War II. The recent developments in IR technology were the results of extensive work done, earlier on Tl_2S, *PbS*, *PbSe*, *PbTe*, *Ge:X*, *Si:X*, *InSb*, *HgCdTe*, *PbSnTe* and *GaAs/GaAlAs*[34]. The focus of interest had been on two atmospheric windows, from 3-5 μm (MWIR) and 8-14 μm (LWIR). Besides, very long wavelength IR (VLWIR) region greater than 15 μm was particularly explored for space applications.

From the point of view of the detector technology, the early detectors based on lead salts were prepared by vacuum evaporation or chemical deposition from a solution. But the phenomenological understanding of these detector materials was rather extremely poor. The narrow gap single crystal detectors from the alloys of III-V, IV-VI and II-VI compounds were aimed at tailor-made bandgap and the approach proved to be very successful. This lead to the emergence of $Hg_{1-x}Cd_xTe$ alloy as one of the most important detector material for MWIR/LWIR as well as VLWIR regions[25,35,36]. Finally, *GaAs/GaAlAs* quantum well infrared photon (QWIP) detectors have been developed taking due advantage of the matured state of *GaAs* technology[34,37-39]. During the 1950s, the single element cooled IR detectors were made usually from lead salt materials. With the development of integrated circuits in 1960s and the availability of photolithographic techniques, multiple element linear array detector technology could become possible, mainly using lead salts and *InSb* materials. The use of extrinsic *Ge:Hg* was made to manufacture forward-looking infrared (FLIR) systems[40] for VLWIR region but with stringent cooling requirement up to 25 K. However, for the intrinsic narrow band gap semiconductors like *HgCdTe*, the cooling condition could be relaxed to higher temperatures in the range 80–200 K. Inspite of the difficulties of growth and fabrication technologies, MCT has the advantage over the other materials in terms of fast response time and compatibility with Si-ROICs. However, MCT photoconductors were not suitable on focal plane arrays due to low input impedance and high power dissipation problems. The 2-D FPAs were, therefore, developed based on photovoltaic detectors for the last more than two decades. Of late since early nineties, the uncooled IR detectors have seized the attention of many workers due to their vast potential for commercial and military applications[41,42].

CT Elliott, a scientist working at the Royal Signals & Radar Establishment, UK, invented a novel IR detector called SPRITE (signal processing in the element) extending conventional photoconductive MCT detector technology by incorporating signal time delay integration (TDI) concept within a single long element. The simple, three-lead structure with a single preamplifier performs the functions of detection and time delay and integration simply

within a filament of *n*-MCT which previously required a number of discrete elements in a conventional serial or serial-parallel scan system with associated amplifiers and time delay circuitry[43,44].

1.4 Relevance of Photoconductive Detectors

For the reasons brought out in Section 1.2, *HgCdTe* photoconductor linear arrays are still in demand and further consolidation of this technology of scanned linear arrays is relevant even today. Several reviews on photoconductors have appeared in the literature from time to time[9,10,12,23,24,26,27,45-48]. Long and Schmit[23] reviewed and concentrated almost entirely on the development of $Hg_{1-x}Cd_xTe$ alloy system as IR detector material. They have also discussed the photoconductive and photovoltaic detector theories applicable to this material and the early developments of detector technology in this area. The brief review by Reine and Broudy[45] was intended to provide basic information on principles of PC and PV detectors operation, the performance characteristics and the summary of the $Hg_{1-x}Cd_xTe$ detector technology. Broudy and Mazurczyk[46] focussed on $Hg_{1-x}Cd_xTe$ photoconductive detector theory, device analysis and design, and briefly discussed the detector processing technology, pointing out key steps involved in array fabrication without elaboration. Elliott[9,10] provided one of the most comprehensive reviews on IR semiconductor detectors.

After a brief survey of the many types of semiconductor detectors, significant details of the theory as well as the limitations and operating characteristics of both photoconductive and photovoltaic detectors of different materials, including MWIR and LWIR $Hg_{1-x}Cd_xTe$ detectors operating at cryogenic and intermediate temperatures have been discussed in this paper. Knowles[12] reviewed the developments in detector technology with emphasis on requirements and operating conditions of IR imaging systems. A summary of $Hg_{1-x}Cd_xTe$ properties for both photoconductive and photovoltaic (approaches to FPA) detectors, detector noise mechanism and performance is presented. There is another quite comprehensive review on intrinsic IR detectors by Rogalski and Piotrowski[26]. The review includes detector theory, crystal growth technology, material properties and detector fabrication technology of different materials including III-V and II-VI. Reine[47] summarised the status of *HgCdTe* IR detector technology, with emphasis on recent developments in *HgCdTe* photoconductor technology for use in the first-generation thermal imaging systems.

There is a comprehensive review on characterisation techniques, both for PC and PV detectors by Reine[48], *et al.* However, there is a clear lack of detailed description of different technological aspects of the device processing in the literature. The main reason behind this deficiency could be due to the strategic or secret nature of the IR technology, developed particularly for military applications, and therefore, the relevant literature is either classified or has limited accessibility. In this review, a sincere effort has been made to bridge this gap with emphasis on photoconductive detector design and processing technology. Therefore, a critical review has been presented on the subject, specifically on the linear array photoconductive detector technology, based on n-$(Hg_{1-x}Cd_x)Te$ material for thermal imaging in 8-12 μm spectral range at cryogenic temperatures.

2. PHOTOCONDUCTIVE INFRARED DETECTORS

2.1 Standard Configuration

The photoconductive detector is essentially a radiation-sensitive resistor. Normally, for large number of photoconductive devices, the device is designed so that electrons dominate the conductivity due to their high mobility, and holes play a secondary role. The operation of a photoconductor is shown in Fig. 1. Photons of energy $h\nu$ greater than the band gap energy E_g are absorbed to produce electron-hole pairs, thereby changing the electrical conductivity of the semiconductor. The change in conductivity is measured by means of electrodes attached to the detector. To sense the change in conductivity, a bias current or voltage is required. Typically, detectors are manufactured in a square or rectangular configuration to maintain uniform bias current distribution throughout the active region. A rigorous theory of photoconductors was given by Rittner[22] to derive and solve a one-dimensional transport equation for photogenerated electrons and holes in a photoconductor. The first results on photoconductivity in $Hg_{1-x}Cd_xTe$

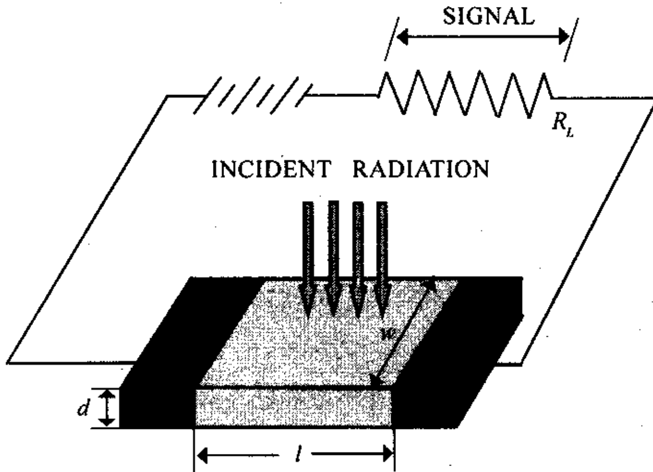

Figure 1. Schematic of a standard photoconductor, showing infrared radiation falling on a slab of detector material having volume *l.w.d* and the signal is measured across a load resistor, R_L.

were reported by Lawson[35], *et al.* in 1959. The Rittner equation had been and remains important in understanding and predicting *n-HgCdTe* photoconductor performance in one dimension[16,49-53]. A comparison of detector performance using both one dimesional and two dimensional models had been reported[54-56]. Gopal[57] discussed the biasing schemes for photoconductors. For low resistance material, such as $Hg_{1-x}Cd_xTe$, the photoconductor is usually operated in a constant current circuit, as shown in Fig. 1. The series load resistor meant to limit the detector current is large compared to detector resistance, and the signal is detected as a change in voltage developed across the load.

2.1.1 *Figures of Merit*

Many different figures of merit are used to characterise or quantify the performance of a detector. These figures of merit enable the user to compare relative performance between detectors. The important performance characteristics of photoconductive IR detectors are as follows:

- *Responsivity*

A basic figure of merit that applies to all detectors with electrical output is spectral responsivity. It is defined as the ratio of photo signal, V_s, of the detector to the incident power, P_λ, of the radiation at wavelength, λ, falling on it. Assuming uniform generation of the photo carriers in the main detector (i.e. *n*-type), and detector thickness, *d*, small wrt. minority carrier diffusion length $L_p=(D_p\tau_p)^{1/2}$, one- dimensional approach was used to study the transport of optically generated electron-hole pairs (Δp = Δn). When the series load resistor, R_L, is large compared to the detector resistance, R_D, a signal voltage across the load resistor is essentially the open circuit voltage. The voltage spectral responsivity, R_λ, is given by[26]

$$R_\lambda = \frac{V_s}{P_\lambda} = \frac{\eta\lambda}{hc}\frac{V_b}{lwd}\frac{(1+b)}{(bn_0+p_0)}\frac{\tau}{\sqrt{(1+\omega^2\tau^2)}} \quad (1)$$

For low modulation frequency ω, $\omega^2\tau^2 << 1$, therefore, can be neglected.

The ratio of mobility of majority carriers, μ_e, to mobility of minority carriers, μ_h, is taken as *b*. It is quite clear from this equation that the basic requirements for high photoconductive responsivity at a given wavelength, λ, are high quantum efficiency, η, long excess carrier lifetime, τ, the smallest possible size of detector (length, *l*, width, *w* and thickness, *d*), low thermal equilibrium concentrations, n_0, and p_0, and the highest possible bias voltage, V_b.

Responsivity varies significantly with active volume of the detector. The optimum system performance is achieved with the smallest size detector capable of collecting the available incident radiation. Responsivity of PC detector is a function of bias. At low bias, the responsivity increases almost linearly with bias. At high bias, self-heating of the detector eventually causes the responsivity to fall. The optimum bias may vary from application-to-application, depending on background radiation levels.

Two material requirements of particular interest in $Hg_{1-x}Cd_xTe$ photoconductors are the electron-doping level and the composition. The doping level is particularly important for the responsivity; lowering the doping level increases the responsivity. Thus, achieving a particular responsivity with a particular detector design requires a doping level less than some fixed value, which depends on the specifications

and design. An important detector parameter called detectivity and cutoff wavelength specifications combine to determine a material composition window. Responsivity for even identical detectors may vary in range over a factor of 2 due to variation in material composition. The specified cutoff wavelength and its tolerance limit determine maximum values of x and Δx for the material to have a band gap small enough to absorb the signal photons.

In case the total blackbody spectrum is falling on the detector, the blackbody voltage responsivity, R_{BB}, would become

$$R_{BB} = \frac{V_s}{P_{BB}} \tag{2}$$

where P_{BB} is the radiant power falling on the detector from the blackbody at a temperature T (normally at 500 K) and modulated at frequency f (normally at 800 Hz). The P_{BB} is obtained by integrating the power over the entire blackbody radiant spectrum and the solid angle of FOV. It may be noted here that when measuring the blackbody responsivity, the radiant power on the detector contains all the wavelengths of radiation and is independent of the spectral response curve of the detector. Some of the wavelengths produce an output and others do not, but the entire flux incident on the detector appears in calculation of blackbody responsivity. In practice, a cold filter with sharp cut-on wavelength and a FOV is desired to reduce the background radiation. The detector material decides the higher wavelength cutoff.

- *Quantum Efficiency*

The quantum efficiency, η, is a very important parameter as it is a measure of how efficiently photons are converted to electrical signal. It is defined as the number of electron-hole pairs generated per incident photon[58]. It depends on absorption coefficient a, thickness d and frontside and backside reflection coefficients[16,58]. Assuming a single pass of the radiation in the detector (shown as a slab of material in Fig.1) and negligible frontside and backside reflection coefficients, the quantum efficiency is

$$\eta = \eta_0\left[1 - e^{(-\alpha d)}\right] \approx 1 - e^{(-\alpha d)} \tag{3}$$

Here, η_0 is the internal quantum efficiency, which can be approximated to unity for direct-band materials. For the ideal situation, the reflection coefficients r_1 and r_2 from front and back surfaces should have values zero and unity, respectively. The quantum efficiency[59] is then given by the following relation:

$$\eta = \eta_0[1 - \exp(-2\alpha d)] \approx 1 - \exp(-2\alpha d) \tag{4}$$

Applying anti-reflection coating on the frontside of the detector, η can be made greater than 0.9.

- *Noise*

Noise refers to an electrical output other than the desired signal. It is undesirable and a considerable effort had been put in to reduce it, as it may obscure or completely hide the small signals. The potential noise sources are fluctuations in the detector itself, in the radiant energy to which detector responds, or in the electronic system accompanying the detector. The detectivity of a detector is limited by noise mechanisms. Usually, the signal and background fluctuations are considered to be responsible for radiation noise. In a photoconductor, the free carriers always exhibit random thermal motion, and because of this, there occurs a fluctuation in the velocity of these carriers, which leads to internal noise. The fluctuations in density of free carriers due to randomness in the rates of thermal generation and recombination also contribute to the internal noise. There can be four different types of internal noise in a photoconductive detector. These are Johnson noise V_j, $1/f$ noise $V_{1/f}$, g-r noise $V_{g\text{-}r}$, and preamplifier noise V_a. Quadratic noise voltage, V_n^2, of a photoconductive detector is composed of these noise factors[46,48], as given below:

$$V_n^2 = V_{g-r}^2 + V_j^2 + V_{1/f}^2 + V_a^2 \tag{5}$$

(a) *Generation recombination (g-r) noise*, $V_{g\text{-}r}$, is due to random fluctuations in the generation and recombination rates of carriers within the detector volume and consists of thermal and background contributions[48], as given below:

$$V_{g-r} = 2eR_D \frac{\mu V_b \tau}{l} \sqrt{lwd(g_{th} + g_b)} \tag{6}$$

$$g_{th} = \frac{p_o}{\tau} = \frac{n_i^2(x,T)}{n_0 \tau} \tag{7}$$

$$g_b = \frac{\eta Q_b}{d} \tag{8}$$

In above expressions, it is clear that a long lifetime is important in reducing thermal *g-r* noise below background *g-r* noise and determines the highest operating temperature at which detector can remain background limited.

The equation for V_{g-r} (in a near intrinsic photoconductor) by simplifying all the terms can be expressed[15] as

$$V_{g-r} = \frac{2V_b}{(lwd)^{1/2}} \frac{(1+b)}{(bn_o + p_o)} \sqrt{\frac{n_o p_o}{(n_o + p_o)}} \sqrt{\frac{\tau \Delta f}{(1+\omega^2\tau^2)}} \tag{9}$$

(b) Johnson-Nyquist noise[46] (thermal noise), V_j is:

$$V_j^2 = 4\, kTR_D\, \Delta f \tag{10}$$

(c) The frequency-dependent noise, $V_{1/f}$ is dominating at low frequencies. The $1/f$ noise is caused by the electronic transitions involving surface states and/or the electrical contacts to the detector. It can often be minimised by appropriate fabrication techniques (by surface treatments or electrical contacting procedures).

(d) The noise contribution of the amplifier can be modelled by the presence of a voltage noise generator of rms magnitude e_a and a current noise generator i_a. The voltage generator is in series with amplifier input, while the current noise generator is in parallel with the input. When a detector of resistance R_D is placed across the input of the amplifier, the noise, V_a generated will be[46]

$$V_a^2 = e_a^2 + i_a^2 \; R_D^2 \tag{11}$$

The measured preamplifier output noise (without a detector at input) of 0.6 nV/Hz$^{1/2}$ is reported recently. This noise is comparable to the 0.5 nV/Hz$^{1/2}$ Johnson noise of a 15 Ω detector resistance[60].

Generation-recombination (*g-r*) noise and Johnson noise are fundamental mechanisms in photoconductors. In the absence of non-fundamental noise, the total noise of the detector, V_n represented earlier by the Eqn (5) would become[15]

$$V_n = \sqrt{(V_j^2 + V_{g-r}^2)} \tag{12}$$

Frequency dependence is related to the lifetime, τ of carriers in the material, and τ depends on material composition and operating temperature[16]. All *HgCdTe* photoconductive detectors exhibit excess low frequency noise which increases approximately as $1/f^{1/2}$ below a certain corner frequency f_c. As frequency is increased above corner frequency, the noise remains constant (called white noise) up to *g-r* cutoff frequency, f_{g-r} which is given by $f_{g-r} = (2\pi\tau)^{-1}$.

The schematic of characteristic noise power spectral density for a photoconductor is shown in Fig. 2. The dominant noise at low frequencies is

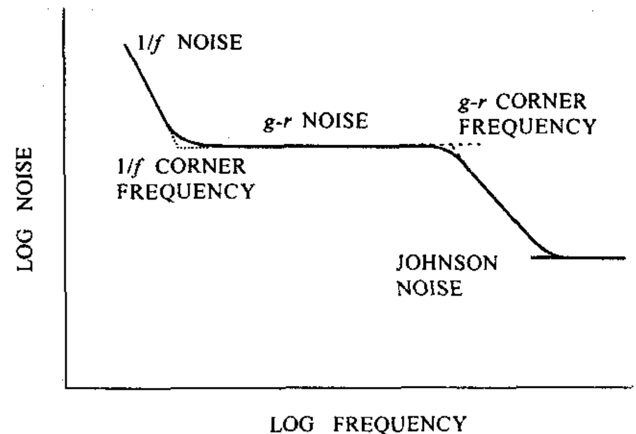

Figure 2. Characteristic noise spectrum of a photoconductive detector. The dominant noise at low frequencies is *1/f* noise, at mid frequencies the *g-r* noise, and at higher frequencies the *g-r* noise rolls-off and Johnson noise is dominant.

$1/f$ noise and at mid-frequencies is the g-r noise. At higher frequencies the g-r noise rolls-off, and Johnson noise is dominant. Discussion on experimentally measured noise of a photoconductive MCT detector is given later.

- *Noise Equivalent Power*

The noise equivalent power of a detector is the minimum required power incident on the detector to produce a signal output equal to the rms noise output. Or in other words, NEP is the power level that produces a signal-to-noise ratio (SNR) of unity.

$$NEP = \frac{V_n}{R_\lambda} \tag{13}$$

It is a useful parameter for comparing the sensitivity of similar detectors that operate under identical conditions and smaller the value of NEP for a detector, higher is its sensitivity. However, conventionally a higher-the-better notion of a quality parameter is preferred. Hence, there was a need for another parameter known as the detectivity to be defined in place of NEP, as the measure of detector sensitivity.

- *Normalised Detectivity*

Normalised detectivity is the most important characteristic of an IR detector meant for various applications. It gives an idea of how much SNR will be obtained by the detector under practical conditions of any application. Normalised detectivity (D^*) is the inverse of NEP normalised over bandwidth and detector area, and is defined by the following relation:

$$D^* = \frac{R_\lambda}{V_n}\sqrt{A\Delta f} \tag{14}$$

Broudy and Mazurczyk[46] gave a comprehensive equation for D^* emphasising how maximum performance represented by D^*_{BLIP} could be modified by other factors as

$$D^* = D^*_{BLIP}\left(1+\frac{p_0}{p_b}\frac{n_0}{n_0+p_0}\right)^{-1/2}\left(1+\frac{f_0}{f}+\frac{V_j^2+V_a^2}{V_{g-r}^2(f)}\right)^{-1/2} \tag{15}$$

At higher temperatures where the detector becomes intrinsic satisfying the condition $V^2_{g-r} >> V_j^2 + V_a^2$ at sufficiently low biases levels, the performance at mid-range frequencies ($f_c < f < f_{g-r}$) is determined by the highly temperature-dependent term inside the first bracket approximating to $p_0/2p_b$. As the detector performance in this range is poor, these approximations are used under the condition when cooling capacity is poor. At lower temperature when semiconductor becomes extrinsic, n_0 becomes constant and dominates p_0, then term inside the first bracket of above Eqn. approximates to $1+p_0/p_b$ and D^* tends to D^*_{BLIP} for the conditions $p_0/p_b << 1$ and $V^2_{g-r} >> V_j^2 + V_a^2$.

At high frequencies $f > f_{g-r}$, amplifier and Johnson noise determine the performance and D^* is given by[46]

$$D^*_{hf} = \frac{R_\lambda(A\Delta f)}{(V_j^2+V_a^2)^{1/2}} \tag{16}$$

The detector range of an infrared imaging system–a very crucial parameter, is proportional to the square root of the detectivity of the detector[5,27].

- *Ultimate Limit of Detection*

An infrared photon detector that achieves background-limited performance is termed background-limited infrared photodetector (BLIP). The performance is limited by the uncertainty in arrival rate of incident photons. The highest performance thermal imagers employ quantum detectors that respond to individual photons. The limit of sensitivity for quantum detectors is determined by the statistical fluctuation in the arrival rate of photons from the scene (background) which, in turn, depends upon the scene temperature and the spectral band being sensed. When the background photon flux is much larger than the signal flux and determines the dominant noise, then

the sensor is in the BLIP mode. For a detector to operate in BLIP mode, the background generation-recombination noise should be much larger than the thermal noise, this sets a lower limit on background irradiance, Q_B. A necessary condition for background-limited operation[9] is that $p_b >> p_0$ or from Eqns (6) to (8)

$$\frac{\eta Q_B \tau}{d} >> \frac{n_i^2}{n_0} \tag{17}$$

$$Q_B = Q_B^0 \sin^2(\theta/2) \tag{18}$$

Q_B^o is the 300 K background irradiance ($\sim 6 \times 10^{17}$ cm^{-2}s^{-1} for 7.5-11.7 μm spectral window). The geometry of the detector and use of cold shield FOV control the background irradiance on the detector. If η = 0.6, d = 10 μm, τ = 2 μs, $n_i = 10^{13}$ cm^{-3}, $n_0 = 5 \times 10^{14}$ cm^{-3}, then the background-limited operation should be observed when $Q_B > 1 \times 10^{15}$ cm^{-2}s^{-1} obtainable using a FOV with $\theta > 5°$ for a background scene temperature[9] of 300 K.

In the advanced infrared detector applications it is usually necessary to approach D^*_{BLIP}. One generally wants to achieve the highest possible value of D^*_{BLIP} by having the quantum efficiency near its maximum attainable value; $\eta \rightarrow 1$. The D^*_{BLIP} can be expressed as[16]

$$D^*_{\lambda\, BLIP} = \frac{\lambda}{2hc}\sqrt{\frac{\eta}{Q_B}} \tag{19}$$

For BLIP operation, the D^* is inversely proportional to the square root of the Q_B. Therefore, by controlling the background irradiance, the D^* of the detector can be improved. Decreasing the number of background photons incident on the detector, each of which contributes to the *g-r* noise, reduces the noise.

Figure 3 shows the variation of D^*_{BLIP} as a function of cutoff wavelength at different background temperatures. Q_B was calculated using equations for spectral radiance of a blackbody[19]. The achievement of background-limited performance depends critically on a suitable technology to produce a low re-

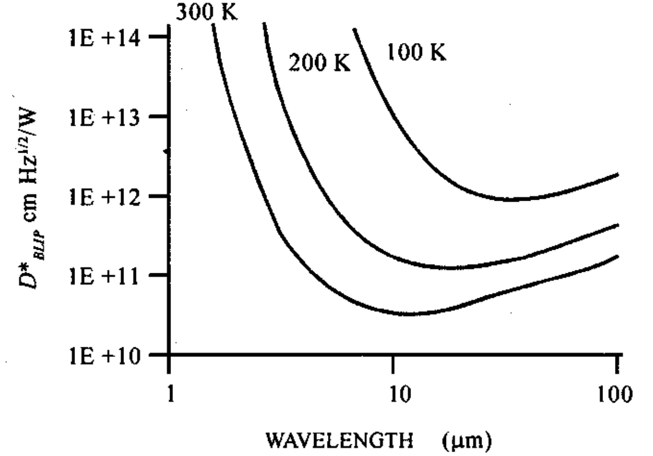

Figure 3. Theoretical values of D^*_{BLIP} at spectral peak for photoconductive detectors viewing a hemisphere surrounded at different background temperatures.

combination velocity at the detector surfaces. The technique, which is commonly used to passivate the surfaces, is anodic oxidation. This results in an accumulated surface at which bands bend, giving an electric field which repels minority carriers from surface recombination sites, thus reducing surface recombination velocities. State-of-the-art cooled infrared detectors are in production at 80-90 per cent of the fundamental limit of D^* in both LWIR and MWIR spectral bands[61].

The above background-limited values of detectivity, D^*_{BLIP} are based upon an optical acceptance angle of 2π steradians, otherwise known as a hemispherical FOV [2π FOV]. In general, it can be shown[3] that

$$D^*(\theta) = \frac{D^*(2\pi)}{\sin(\theta/2)} \tag{20}$$

The limiting D^* in the zero background flux which can be obtained in large detectors[62] is:

$$D^*_\lambda = \frac{\eta\lambda}{2hc}\left(\frac{2\tau_{Ai1}}{n_0 d}\right)^{1/2} \tag{21}$$

where τ_{Ai1} is the intrinsic Auger 1 lifetime which has a value of approximately 1 ms, and taking all other values as above

$$D^{*}\lambda = 2.2 \times 10^{12}.\ \eta \qquad (22)$$

The agreement is excellent with D^* values of well over 10^{12} cm $Hz^{1/2}W^{-1}$ in the liquid nitrogen temperature[62].

- *Gain*

The photoconductive gain, g, is defined as the number of carriers passing through the contact per each generated electron-hole pair. This gain describes how efficiently the generated electron-hole pairs are used to create electrical signal. Since, in general $\mu_e > \mu_h$, the photogenerated electrons traverse through the semiconductor much faster than holes. To preserve charge neutrality, and for current continuity, the external electrode must, therefore, supply electrons from the opposite side. These new electrons may travel faster across the detector than the original holes and cannot recombine with them. If this happens, a gain is produced which is proportional to the number of times an electron can transit the detector within its lifetime. Typical gain, g, can be written as a function of lifetime of minority carrier, τ, and transit time of electron across the detector, t_d:

$$g = \frac{\tau}{t_d} \qquad (23)$$

- *Crosstalk*

In case of an array of detectors, when the image is focused on one single detector, there should be no signal from other detectors. But practically, some signal will be present on other adjacent detectors, although it should be very small. This excess signal is known as the crosstalk. It is generally measured as a percentage of the output or driving signal. A requirement of crosstalk less than 5 per cent can be easily met but values less than 0.05 per cent are hard to meet. Crosstalk can be due to the optical effects (eg, reflections from the detector on which the image is focused) and the electrical effects (eg, capacitive coupling between the signal leads). This effect becomes very important when designing an array with closely spaced detectors and will put a limitation on the detector size and the pitch[13].

2.2 SPRITE–Photoconductive Alternate to Focal Plane Array

The signal processing in the element (SPRITE) detector was originally invented by CT Elliott and developed further virtually exclusively by British scientists[43,44,63-74]. It is a highly sensitive IR detector, which facilitates TDI function in a single strip of n-type $Hg_{1-x}Cd_xTe$. This device is applicable to a serial or serial-parallel thermal imaging first-generation systems. The major advantage of the device is in considerable simplification of the off-focal-plane electronics with consequential benefits in size, weight, and reliability of the systems.

The relatively smaller number of leads and interconnects needed per unit area of the detector stripes on focal plane makes it attractive for large arrays. The device was conceived as an alternative approach to hybrid FPAs employing charged coupled devices (CCDs)/complementary symmetry metal oxide semiconductor (CMOS) readout integrated circuits (ROICs). As it does not suffer from charge storage limitations of CCDs, the device is particularly suitable for LWIR band. Also since intrinsic photoconductive mode is employed, the SPRITE detector, in principle, can operate at higher temperatures than extrinsic silicon IRCCDs.

The detector, as illustrated in Fig. 4, consists of a strip of IR-sensitive material (generally n-type photoconductor) on a sapphire substrate[43]; it has only three electrical connections, i.e., two bias contacts and a readout potential probe. These detectors are used extensively in high performance thermal imaging systems. If a small area of the strip is exposed to IR radiation, excess current carriers are generated within that region.

These carriers drift towards the readout area of the strip at a velocity determined by the bias current and matched to the velocity at which the target image scans the strip, v_s. Consequently, the excess carriers are swept along the strip together with the target image. In this way, the accumulated carriers arrive at the readout area at the same time, eliminating the need for the external delay and summation circuitry, and reducing the pre-amplifier output connections to one.

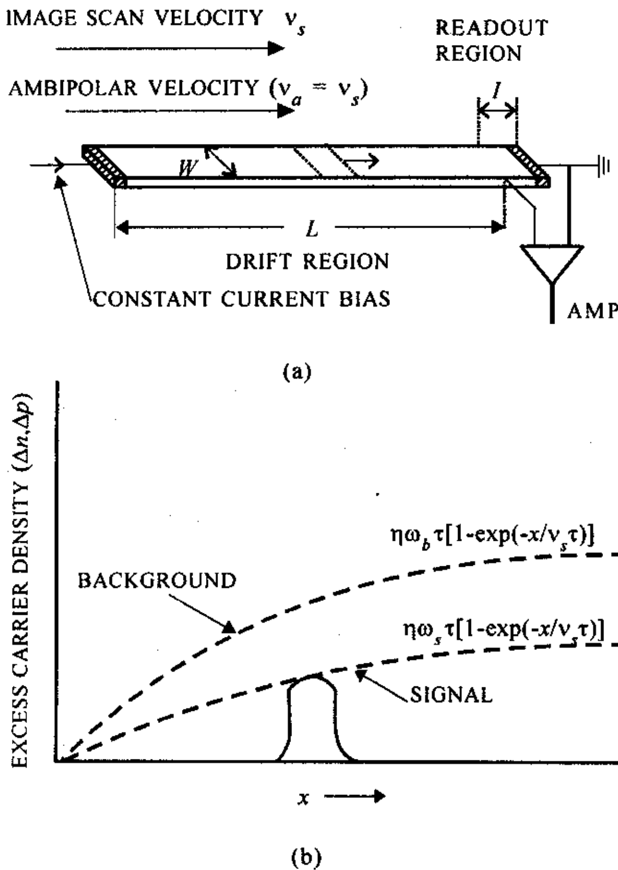

Figure 4. The operating principle of a SPRITE detector: (a) an MCT element with three Ohmic contacts, and (b) the build-up of excess carrier density in the device as a pixel of the image is scanned along it. The movement of image matches the drift of minority carriers along SPRITE filament.

The length of the detector, L, is typically close to or larger than the drift length $v_d\tau$, where τ is the recombination time. The excess carrier concentration in the material increases during scan. When the illuminated region enters the readout zone, the increased conductivity modulates the voltage on the readout contact and provides an output signal. The integration time approximates the recombination time τ for long detectors. It becomes much longer than the dwell time τ_{pixel} on a conventional element in a fast scanned serial system. Thus, a proportionally larger ($\propto \tau/\tau_{pixel}$) output signal is observed. Therefore, the SPRITE detector continuously performs a TDI function and the SNR is improved as a result of coherent integration of signal and incoherent integration of the noise. In the background-limited detector, the excess carrier concentration due to background also increases by the same factor, but corresponding noise is proportional only to integrated flux. As a result the net gain in the SNR wrt to a discrete element is increased by a factor $(\tau/\tau_{pixel})^{1/2}$.

D^*_λ can be expressed in terms of pixel rate, s, which, for a nominal resolution size of $W \times W$ is v_s/W, then in the high scan speed limit

$$D^*_\lambda = (2\eta)^{1/2} D^*_{BLIP} (s\tau)^{1/2} \tag{24}$$

The performance of the SPRITE device is thus equivalent to a serial array with the number of BLIP-limited elements ($N = 2s\tau$). For example, in a system with a 4 MHz pixel rate and assuming $\tau = 2$ µs, the simple three lead structure with a single preamplifier should give equivalent performance to a serial row of 16 background-limited photoconductive detectors with 16 preamplifiers and the associated delay circuits[64].

The material requirements for the device are determined by the need for large lifetime τ to provide long integration, and low minority carrier diffusion length to provide good spatial resolution. The diffusion-limited resolution size is approximately twice the diffusion length.

Parallel arrays of SPRITE can be substituted for discrete element arrays in serial parallel imaging systems[43]. The principal benefit of SPRITE in systems has been in simplification of the electronics and gain in detectivity. Two major advantages of these close-packed two-dimensional devices are: (i) significant reduction in the number on interconnects as compare to conventional array and (ii) the high responsivity levels which facilitate the fabrication of low power consumption buffer amplifiers.

3. DETECTOR DESIGN: SOME CRITICAL ISSUES

Quality performance not only demands optimum sensitivity, it also mandates product reliability. Surface passivation, contact metallisation and reliability of

wire bonding are the three main factors affecting the stability of the MCT detector. Detectors are designed keeping in view all the unit processes, which are responsible for achieving the desired detector parameters. Some of the important issues related to detector design are discussed below:

3.1 Diffusion & Drift Effects

Equation (1) shows that R_v should increase monotonically with the V_b. However, there are two limits on applied bias voltage, thermal conditions, i.e., Joule heating of the detector element, and the sweep-out of minority carriers. The effects of contacts and of drift and diffusion of excess carriers cannot be ignored. For small detectors used in high resolution thermal imaging systems with $l < 50$ μm, the minority carriers can drift to Ohmic contacts even at moderate bias field (Fig. 5), in a time short compared to recombination time in the detector material. Removal of minority carriers at an Ohmic contact in this way is called the sweep-out effect[15,50,75-79].

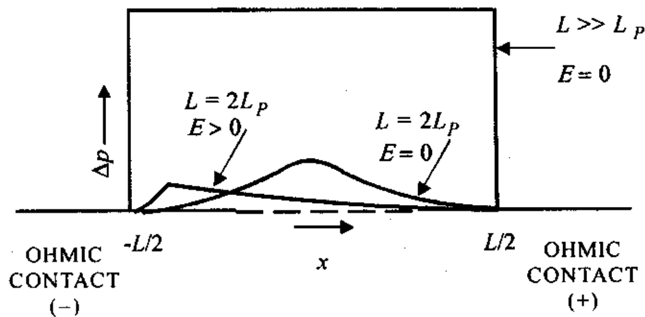

Figure 5. Excess carrier distribution in a detector element with Ohmic contacts: At $E = 0$, it is uniform for $L >> L_p$ and significantly reduced with symmetric bell-shaped for $L \leq 2L_p$. At $E > 0$ and $L \leq 2L_p$, it gets skewed towards cathode.

This results in reduction of responsivity and generation-recombination noise and also limits the maximum applied voltage, V_b. Because the rate of reduction of the generation-recombination noise is lower than that of the responsivity, it results in reduction of detectivity.

The loss of detectivity is especially significant when the Johnson noise becomes dominating due to reduction of generation-recombination noise. For moderate sweep-out conditions, the detectors exhibit the generation-recombination noise/sweep-out limited detectivity. When the generation-recombination noise is reduced below the Johnson noise, the detectivity becomes Johnson noise/sweep-out limited.

The effective carrier lifetime can be reduced considerably in detectors where the minority carrier diffusion length exceeds the detector length, L_p. At higher values of the applied field, the drift length of the minority carriers is comparable to or greater than L_p. Some of the excess minority carriers are lost at an electrode, and to maintain space charge equilibrium, a drop in excess majority carrier density is necessary. This way the majority carrier lifetime is reduced. The lifetime degradation problem is associated with Ohmic contacts and can be minimised using: (i) an extended (overlap) structure and (ii) blocking contacts (Hi-Lo or heterojunction). Sweep-out significantly reduces detector responsivity and increases the material and temperature requirements necessary for the detector to achieve background-limited detectivity.

Various workers[15,50,75-79] have carried out analysis of the influence of the sweep-out on photoconductor performance. The expressions for voltage responsivity, noise and normalised detectivity are applicable, if the term for lifetime, τ is modified[15] by τ_{ef}

$$\tau_{ef} = \tau\left[1 - \frac{\tau}{\tau_a}\left\{1 - \exp\left(\frac{\tau_a}{\tau}\right)\right\}\right] \quad (25)$$

$$\tau_a = \frac{l^2}{V_b \mu_a} \quad (26)$$

When the material is close to intrinsic or the background flux density is very high, $n \approx p$ and $\mu_a \approx 0$. For n-type photoconductors with a large mobility ratio ($b >> 1$) and $n >> p$, Eqn (25) becomes[15],

$$\frac{1}{\tau_{ef}} = \frac{1}{\tau} + \frac{2}{\tau_a} \quad (27)$$

Modifications of standard device geometry have been discussed as an approach to reduce the undesirable effects of carrier sweep-out on device performance.

Use of asymmetrical overlap on cathode side and the n-n^+ blocking contacts can reduce these undesirable effects. Both of these features enhance the effective lifetime of the carriers without compromising the resolution.

3.2 Contact Schemes

3.2.1 *Extended/Overlap Contacts*

The Ohmic contacts are regions of high recombination. It is, therefore, desirable to isolate the contact regions from active area boundary. In the extended/overlap configuration, the distance between these electrical contacts is extended to L beyond the active window length l without compromising active window size (and resolution), and thus increasing the minority carrier transit time, τ_a. An optical mask is used to define active area to achieve required spatial resolution. The advantages of such a structure compared to a conventional photoconductor can be realised by a simple analysis of the voltage responsivity of the overlap detector.

For a conventional photoconductor with zero applied bias field, and for detector length, l, much more than minority carrier diffusion length, L_p, the signal photon flux, ϕ, generates a virtually uniform density of excess minority carriers along the length. As the detector length approaches minority carrier diffusion length, the distribution of excess minority carrier significantly deviates from uniform profile across the detector length to non-uniform profile with zero carriers at the contacts and the density of excess carrier at the centre of the detector element also decreases, as it is now less than the diffusion length away from the contacts. Further deterioration of this situation occurs, when an electric field is applied, and sweep-out of minority carriers takes place. The excess carrier density is further reduced and the distribution is skewed towards the negative electrode. This phenomena was analysed by Rittner[22] and the excess minority carrier density, Δp at any point x along the detector element is given by[79]

$$\Delta p = \frac{\eta \varphi_s}{d} \tau_p \left[1 + \frac{e^{\alpha_1 x} \sinh \alpha_2 l/2 - e^{\alpha_2 x} \sinh \alpha_1 l/2}{\sinh(\alpha_1 - \alpha_2) l/2} \right] \quad (28)$$

where $$\alpha_{1,2} = \frac{\mu E}{2D} \pm \left[\left(\frac{\mu E}{2D} \right)^2 + \frac{1}{D\tau_p} \right]^{1/2} \quad (29)$$

For the purpose of analysis, the effective lifetime may be defined by

$$\tau_{eff} = \tau_p \left[1 - \frac{1}{\cosh(l/2L_p)} \right] \quad (30)$$

For large values of detector length, l, the effective lifetime approaches the bulk lifetime. However, as l approaches L_p, the effective lifetime decreases rapidly and for $l = L_p$, the value of τ_{eff}/τ is approximately 0.1.

Figure 6 illustrates the variation of effective lifetime versus detector length for various values of bulk lifetime. It is apparent that for lower geometry detectors a serious problem of lifetime degradation exists, with values of τ_{eff} limited to $\leq$ 650 ns, even for τ as high as 8 µs.

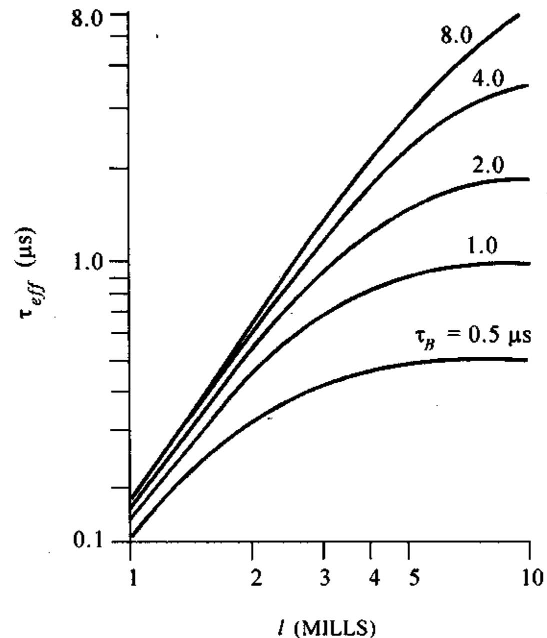

Figure 6. Variation of effective lifetime versus detector length for various values of bulk lifetime. τ_{eff} is strongly dependent on detector length (< 75 µm). τ_{eff} is reduced to $\leq$ 650 ns even for a good lifetime bulk material.

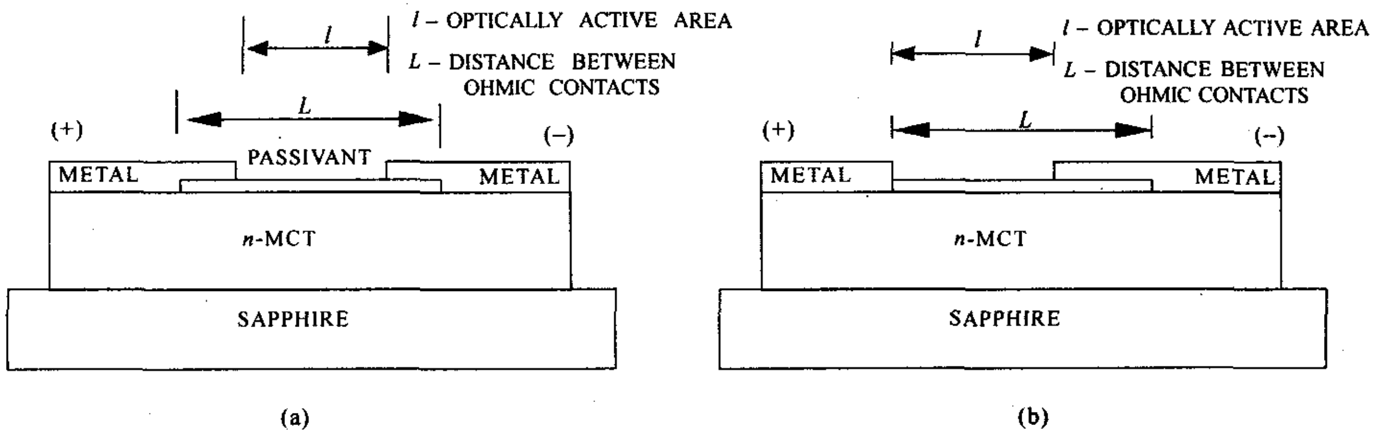

Figure 7. (a) Schematic of symmetric overlap structure, the distance between Ohmic contacts, L is more than the length of active area, l and (b) maximally asymmetric overlap structure, it yields optimum performance enhancement.

This problem is further compounded for 0.1 eV detectors that are required to operate at near-ambient background photon fluxes. Under such conditions, the Auger mechanisms limit the attainable bulk detector lifetime[79] to values of $\tau_p \leq 1$ µs. For example, for a detector of length 50 µm this results in the values for $\tau_{eff} \leq 400$ ns.

This degradation of lifetime can be reduced by a modified geometry of the detector as shown in the Fig. 7(a) for a symmetric overlap structure. Where the Ohmic contacts, shown at a distance L apart, do not define the optically active area of the detector, which has a comparatively lower dimension l. This optically active area is defined by a metal overlay of the insulating passivant layer. Thus, the optically active volume is displaced from the Ohmic contact regions with their associated high recombination velocities. The photo-signal associated with a signal flux density of ϕ_s photons/cm^2 s for a signal power[79] $\Delta W = \phi_s h\nu l w$ is given by the equation:

$$\Delta V = V\frac{\Delta N}{N} \tag{31}$$

where $\Delta N = \eta\phi_s\tau_{eff} lw$

and $N = n_o Lwd$

therefore, $$\Delta V = V\frac{\eta\phi_s\tau_{eff}}{n_o d}\times\frac{l}{L} \tag{32}$$

The detector voltage responsivity R_λ *variation* with detector element length, L, is of prime importance while bias power is held constant. For signal power $\Delta W = \phi_s h\nu l w$ and constant bias power $P = V^2/R'$, where R' is the detector resistance per unit length, the voltage responsivity is given by

$$R_\lambda = \frac{\Delta V}{\Delta W} = \frac{(PR')\eta}{n_o h\nu w d}\frac{\tau_{eff}}{L^{1/2}} \tag{33}$$

The effective lifetime increases as a function of L^2 up to values of L satisfying the condition $L/L_p \sim 5$. Beyond this, effective lifetime increases as a function of $L^{1/2}$. The detector length, therefore, can be increased up to approximately five times the minority carrier diffusion length with enhancement of voltage responsivity at constant detector bias power.

For operation in the sweep-out limit, the effective lifetime is equivalent to the transit time for photo-generated disturbance across the detector element, and for a symmetric overlap structure $\tau_{eff} \cong L^2/2\mu V$. For a grossly asymmetric overlap geometry, as shown in Fig. 7(b), $\tau_{eff} \cong L^2/\mu V$. Then, for near intrinsic material or detector operating under high background fluxes such that $p_0 \to n_0$ the responsivity will show a further increase.

In comparison to standard structures, the overlap structures offer several advantages, such as: (i) reduced responsivity saturation with increasing field,

(ii) lower D^* dependence on field, and (iii) reduced $1/f$ noise corner frequency but only marginally affecting response time constant. However, the increased detector length increases both the detector power dissipation and noise at a fixed bias. Thus, there is a severe limit to how much the length can be increased and by what factor an increase in responsivity can be achieved. Kinch[79], *et al.* estimated the critical detector element length associated with thermal D^* improvement to be approximately three times the minority carrier diffusion length. A comparison of standard versus overlap structures is summarised in Table 2.

Table 2. Figure of merits for standard versus overlap structures

Figure of merit	Standard	Overlap
Responsivity (R_v)	Sweep-out saturation ($R_{v\ std}$)	No sweep-out saturation ($1.25 - 5.0 \times R_{v\ std}$)
Detectivity D^*	Fast decrease with E (D^*_{std})	Very slow decrease with E ($1.2 - 2.5 \times D^*_{std}$)
$1/f$ corner frequency	Fast increase with E ($f_{c\ std}$)	Fast increase with E ($< 1/3 \times f_{c\ std}$)
Resistance	Low (r_{std})	High ($3.0 - 5.0 \times r_{std}$)
Response time	Low	High

3.2.2 *Blocking Contacts*

In a conventional photoconductor, two Ohmic contacts are applied at the ends of the semiconductor slab. According to the definition of an Ohmic contact, the excess carrier density at the contacts is zero, or the surface recombination velocity is infinite, which leads to drastic reduction in effective lifetime of the carriers. To enhance the lifetime, the contacts of carrier blocking or reflecting type are desirable. The n-n^+ blocking contacts create a barrier to the flow of minority carriers while offering no resistance to the majority carriers[80-82]. This decreases the recombination velocity at the contacts, S_{srv}, which effectively increases the lifetime of the carriers. Kumar[81,82], *et al.* examined the relationship between contact recombination velocity and the n^+/n blocking contact structure. For a given carrier recombination velocity at the metal-semiconductor interface, both the doping ratio of the n^+/n region and the thickness of the n^+ region need to be optimised to improve the detector performance.

In the case of blocking contact, the photo-generated electron-hole pairs are not annihilated in the immediate vicinity of the metal-semiconductor contact. Such a contact may be partially or even totally reflecting minority carriers as a result of built-in electric field opposing the collection of minority carriers at contacts. In the case of total reflection, the electron-hole pairs are virtually forced to recombine eventually in the bulk of the semiconductor, due to finite lifetime, and the responsivity is modified accordingly. The built-in electric field results from a decreasing majority carrier concentration profile, from the metal contact into the semiconductor bulk.

The detectivity decreases as intrinsic carrier concentration, N_i, is increased for all values of surface recombination velocities, S_{srv}. This decrease in D^* is the result of increased free-minority carriers, leading to increased thermal g-r noise. The rate of decrease of D^* with N_i is much less for detectors with small value of S_{srv} than for Ohmic contact detector. For the highly blocking contact detector (also longer effective lifetime) when the background g-r noise dominates the thermally generated contribution, the effect of N_i on D^* is relatively less. In comparison to Ohmic contacts, the blocking contacts[51] enhance responsivity and D^*, allow to use material with higher carrier concentration and wider compositional variations, Δx. These features have led to improved D^*, R_v, lower $1/f$ noise corner frequency and other benefits in the fabricated arrays[51,83-85]. Contacts can be formed on n-MCT by either creating an Hi-Lo n-n^+ barrier (by indium diffusion[86] or ion beam milling[87,88]) called Hi-Lo blocking contacts (HLBCs) or by forming heterojunction barrier called as heterojunction blocking contact (HJBC).

3.2.2.1 Hi-Lo *Blocking Contacts*

(a) *HLBC by Diffusion*

Indium is frequently used as contact metal in n-type MCT photoconductive detectors to form Ohmic contacts, During the low-temperature annealing cycle of device processing technology the indium present at the contacts diffuses into the lattice. Concentration gradients and consequently built-in electric field of 10-20 eV cm^{-1} at 77 K are formed[86]. These fields modify the distribution and surface

recombination velocity of photo-excited carriers. Excess photo-excited minority carriers are pushed away from the surface and electrons are attracted towards it[89]. An n-type photoconductor with heavily doped-end regions is shown in Fig. 8.

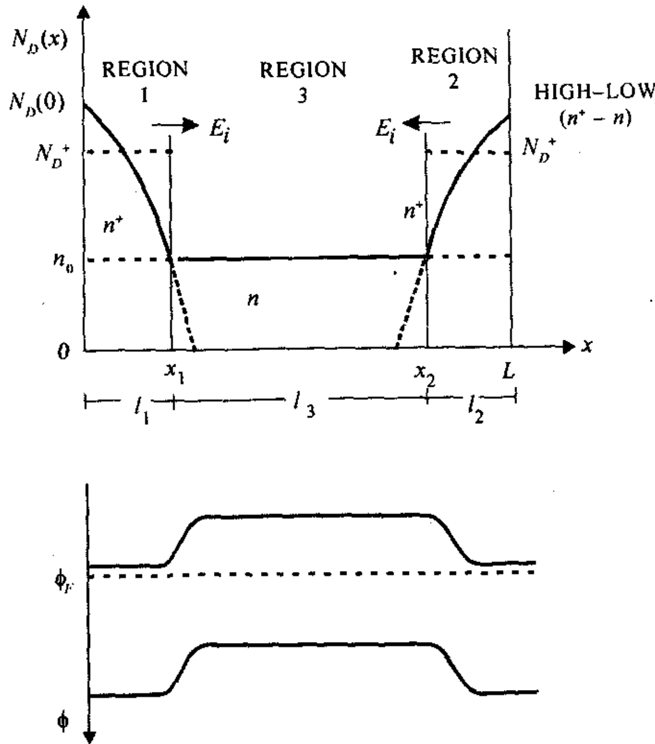

Figure 8. Impurity profile and corresponding energy diagram of one-dimensional n-type photoconductor with heavily doped n^+ contact regions. The optical excitation occurs in region 3. The n^+ regions ($l_1 = l_2 << l_3$) are approximated by a uniform step junction profile with constant electron concentration N_D^+.

The excess majority carriers in the vicinity of the contacts result from in-diffusion of donor during the processing of the device. Accordingly, the device is divided into three regions, with optical excitation taking place in the central region 3 only. It must be emphasised that $l_1 = l_2 << l_3$. As a result of this majority carrier profile, an internal electric field E_i, must exist in the above regions, in addition to any applied field. This is equivalent to an energy barrier[89] ΔE, which is given by

$$E_i \cong \left(\frac{kT}{q}\right)\left(\frac{1}{N_d(x)}\right)\left(\frac{dN_d}{dx}\right) \quad (34)$$

$$\Delta E_i = kT \ln\left(\frac{n^+}{n}\right) \quad (35)$$

The direction of this internal field is such as to oppose collection of minority carriers (holes) by the metal contacts (at coordinates 0 and l). Majority carrier electrons are nearly unimpeded by such contact. This results in reduction in the recombination velocity of photo-generated holes and increase in effective lifetime. The measured effective lifetime of holes increases approximately by a factor of two. A comparison of various figures of merit of detector for Ohmic versus blocking contacts is presented in Table 3.

Table 3. Figure of merits for Ohmic versus blocking contacts

Figure of merit	Ohmic/ Standard	Blocking contacts
Responsivity (R_v)	$R_{v\ std}$	$3.0 \times R_{v\ std}$
Detectivity (D^*)	D^*_{std}	$1..5 \times D^*_{std}$
Carrier conc. range (cm^{-3})	$< 4 \times 10^{14}$	$4 - 20 \times 10^{14}$
Composition variation ($x = 0.2$)	± 0.006	± 0.012
Response	Fast	Slow

However, obtaining reproducible clean MCT surfaces in the contact regions of an array before metallisation is quite a challenging task. Also, it has been observed that indium contacts degrade as a result of thermal annealing. Gold used for fanout pattern and contact indium form an intermetallic compound, which modifies the contact resistance to the extent that the total detector/contact impedance become unstable with time, leading to long-term reliability problem of the device. Therefore, the alternate metallisation schemes such as *Cr-Au* or *Ti-Pt-Au* have to be used to address the long-term reliability issues.

(b) *HLBC by Milling*

Work on MCT surface modification and conversion of p-type MCT to n-type and n-type to n^+-type by low energy ion bombardment was reported earlier by some workers[87,88,90-94]. A detailed study of the dependence of the conversion depth profiles on ior

beam milling conditions was presented recently by Mittal[95], *et al.* The depth to which these changes occur depends strongly on ion milling conditions. The local damage due to impinging ions is restricted to a distance of the order of the ion interaction range, while the converted zone is much deeper. The rapid diffusion of mercury freed from the lattice is believed to be the cause of junction formation. Many authors[88,90-92,94] have reported detailed discussions on junction formation for p-type MCT. However, very few reports are available on the effect of ion beam etching on n-type *HgCdTe*. To select the ion beam current density and etch time for proper junction formation, a detailed study of the carrier concentration profile of n^+/n junctions induced by ion milling process under different process conditions was carried out by differential Hall measurements[95-97]. The depth of modified region increases almost linearly as a function of ion dose. Formation of a strong n-doped region is observed even for very small milling doses. The increase in the ion dose (beam current × etch time) results in an increase in carrier concentration for these samples by 3–4 order over the base carrier concentration values of 2–4 × 10^{14} cm^{-3}.

Blackman[88], *et al.* have shown that the volume, V, of converted material follows a simple law:

$$\frac{dV}{dt} = k\frac{G}{N_a} \tag{36}$$

If t is the time of bombardment and A is the area, then the junction depth, d, for large area is given by

$$d = \frac{k\ G\ t}{N_a\ A} \tag{37}$$

where $(G / A) = J$, is the current density, and $G \times t$ is defined as the ion dose.

Mittal[95], *et al.* have shown experimentally that the similar theory (as given for p-type material) holds good for n-type material also, the integrated ion dose is an important parameter, as reported earlier. The change in carrier concentration tends to saturate at an ion dose of 8 × 10^{18} ions/cm^2, but the converted region depth increases linearly with ion dose, for constant beam energy.

Type conversion is found to take place rather too fast and deeper than expected from the process of chemical diffusion of *Hg* in *HgCdTe*, especially when the sample is cooled to about 13 °C during milling. The milling process etches out the top layer from *HgCdTe* sample by the sputtering process as a result of momentum transfer by bombarding ions to the lattice atoms. Due to non-stoichiometric etching, free *Hg* atoms are left on the surface. The energetic bombarding Ar^+ ions may transfer their kinetic energy during collision to the free *Hg* atoms (in the direction of lattice), thus resulting in-diffusion of these as *Hg* interstitials at a diffusion rate much higher than predicted thermodynamically. In addition, collision of Ar^+ ions with lattice atoms in the sample creates the Frenkel defects (mercury interstitial-vacancy pair) and loosing their energy in the process. The amount of free *Hg* atoms generated within the etched region during milling would depend on ion dose. The junction depth, in turn, is a complex function of the amount of free *Hg* atoms, their kinetic energy, etc. The qualitative explanations and models presented so far are insufficient to predetermine the depth profile and junction depth of the converted region.

It is pointed out here that the increased detector length in the extended contact scheme increases both the detector power dissipation and noise at a fixed bias. In the n/n^+ contact scheme, an energy barrier to minority carriers is generated in front of metal by heavily doping of this region. The lifetime in heavily doped region severely degrades due to Auger recombination, limiting its effectiveness. Thus, both the extended contact scheme and the blocking contact scheme can lead to increased responsivity, but neither scheme eliminates sweep-out nor is close to an optimal approach. In all the three approaches used to lower sweep-out effect, the maximum increase in responsivity is approximately a factor of five[79,98]

(ii) *Heterostructure Blocking Contacts*

Honeywell Group[51,83,84] presented an experimental and theoretical study of n-type $Hg_{1-x}Cd_xTe$ heterostructure photoconductors in which a non-

absorbing large band gap alloy was grown on top of a smaller band gap active region. The contacts were made to the larger gap material. The larger band gap material causes an energy barrier to holes, which decreases the rate at which they reach the high recombination region of the metal-semiconductor interface. As a result, this heterojunction contact greatly reduces the effects of carrier sweep-out on device performance and leads to much higher detector responsivities. As an example, for $Hg_{1-x}Cd_xTe$ photoconductors made from lower narrow gap layer with $x \approx 0.2$ and a larger band gap top layer of $x \sim 0.24$, the barrier height with this $\Delta x = 0.04$ is about 9 kT. This barrier is 2-3 times that is achieved in the Hi-Lo junction[51,83-85]. Both the layers are n-type having approximately similar doping densities and heterojunction interface is graded over a larger depth compared to depletion width. The energy barrier, approximately equal to the band gap difference of 0.04 eV, occurs in the valence band, as shown in Fig. 9. When an electric field is applied, photogenerated minority carrier holes encounter a potential barrier at the heterojunction

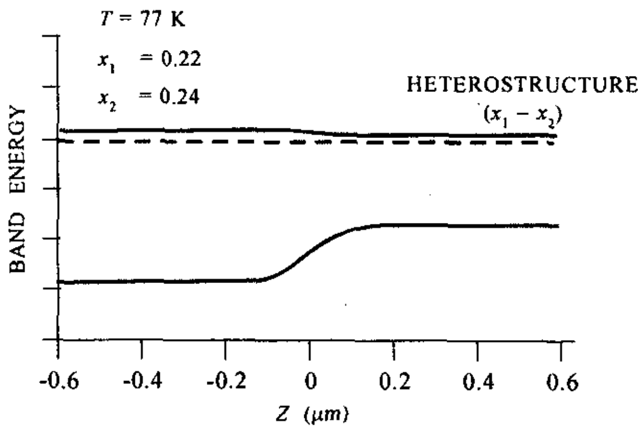

Figure 9. Energy band diagram for an n-n^+ heterostructure with $x_1 = 0.220$ and $x_2 = 0.240$.

interface, which prevents these from reaching the metal/semiconductor interface, thus effectively reducing the sweep-out effects. However, virtually no barrier exists for electrons. Thus, the barrier reduces the rate at which minority carriers are lost at the metal-contact, which, in turn, results in decrease in surface recombination velocity and increase in the effective minority carrier lifetime. Consequently, responsivity and background generated g-r noise, both increase and detectivity is pushed toward the background limit. At higher applied bias fields, the responsivity of HBC photoconductors improves in comparison to Hi-Lo junction photoconductors.

Musca[85], *et al.* have used more practical approach to analyse HBCs, assuming a finite recombination rate at metal/semiconductor interface and presence of recombination centres at hetero-interface (due to lattice stress because of change in the lattice constant). Also, the surface shunting of detector due to the presence of either a wider band gap capping layer and/or passivation layer at the surface of the semiconductor active layer has been taken into account. It is very much clear that by applying HBC, the recombination velocity decreases and the effective lifetime increases. Change in these two factors in a one-dimensional model [Eqn (1)] can explain both Hi-Lo and heterostructures. Responsivity increases by a factor of two for photoconductors with heterostructures as compared to the ones with Hi-Lo contacts. Also, the improvement in responsivity is more than an order of magnitude at low-bias fields in a near ideal HBC photoconductors as compared to devices with non-blocking Ohmic contacts.

3.3 Detector Resistance

In its simplest form, the n-type MCT photoconductor consists of a rectangular piece of material of thickness d, with an active area defined by the width, w, and the electrode length, l, as shown in Fig. 1. The detector resistance, R_D, is given by

$$R_D = \frac{1}{n_0 e \mu_e} \frac{l}{wd} \tag{38}$$

Usually there is a surface accumulation layer placed over the surfaces of the $HgCdTe$ for passivation purposes. Passivation reduces surface recombination and $1/f$ noise and renders the surface impervious to environmental conditions. For example, anodic oxide can be used for this purpose. The positive fixed charge in the oxide layer produces a strong accumulation layer[99,100] on n-type $HgCdTe$. This accumulation layer has an electrical resistance that adds in parallel to that of the bulk $HgCdTe$ material.

If n_s is the density of surface electrons in the accumulation layer and μ_s is their mobility, then the detector resistance becomes

$$R_D = \left(\frac{1}{e[n_o\mu_e + (2n_s\mu_s / d)]} \right) \left(\frac{l}{wd} \right) + 2R_c \tag{39}$$

where R_c represents contact resistance[48]. Contact resistance in *n*-type *HgCdTe* photoconductors has two origins: (*i*) *interface resistance between the* contact metal and the *HgCdTe* material, and (ii) the current crowding that occurs when the direction of the current changes from parallel to the detector surfaces to perpendicular to the contact surface. *Usually the contact resistance term is* small (10-15 Ω) compared with the *HgCdTe* material and surface terms and in most cases, the contact resistance has no deleterious effect on device performance[48,101].

Room temperature detector resistance (RTR) measurements can be used as the first criterion in the selection of good detectors for further characterisation at low-temperature measurements. Uniform resistance values (close to the calculated detector resistance plus two times R_c, with R_c~10-15 Ω) at room temperature across the array indicate no failure at device processing stage. Then, the low-temperature resistance (LTR) *measurements* give an idea about the quality of detector material and contacts.

It has been observed from our experience that for detectors showing high responsivity, low noise, and high detectivity, the value of LTR/RTR ratio should be around two. The large increase in this ratio beyond two is an indicator of either the poor adhesion of the metal contact to *HgCdTe* that is adversely affected by thermal cycling or caused by damage to the material. Also, the improper metal step coverage on the *HgCdTe* slope while the contact runs down to the epoxy/sapphire can also contribute to such phenomenon. Pal[102], *et al.* had performed detector-resistance measurements at 77 K for variable incident flux on the detectors and from these measurements calculated the values of contact resistance, shunt resistance, and $\eta\tau$ product. Variations in shunt resistance and $\eta\tau$ product can lead non-uniformity in the responsivity, while high values of contact resistance can lead to degradation in the D^* and also adds to the cooler heat load.

3.4 Surface Recombination Velocity

In a thin *HgCdTe* photoconductor, the surfaces are very near to the excess carriers, therefore recombination at these surfaces can limit the attainable lifetime. If τ_{bulk} is the *HgCdTe* lifetime, then the resulting lifetime with surface recombination is[48]:

$$\frac{1}{\tau_{net}} = \frac{1}{\tau_{bulk}} + \frac{2S_{srv}}{d} \tag{40}$$

where S_{srv} is the surface recombination velocity. A value of S_{srv} as small as 500 cm s^{-1} would limit the lifetime of carriers in a 10 μm thick detector to 1 μs. Also, the recombination at the contacts can be important in many cases.

At large values of S_{srv}, the responsivity saturates with increasing bias field because the effective lifetime becomes an average carrier transit time. As the contact recombination velocity is decreased, the effective lifetime is limited by the rate of hole passage into the contact rather than the rate of transport to the contact. Smith[51] has shown the variation of responsivity, noise and detectivity at low frequency as a function of applied bias field with surface recombination velocity as a parameter. Both responsivity and noise increase rapidly as S_{srv} is decreased below a few thousand centimeter per second. Thus, the maximum value of responsivity increases as S_{srv} is decreased. If the limit $S_{srv} \rightarrow 0$ is taken, the holes cannot pass into the contact at all, and the responsivity does not saturate with increasing bias field but continues to increase linearly.

The generation-recombination noise at large S_{srv} does not saturate with increasing bias but increases like $\sqrt{E}$, when there is a large thermal generated contribution to the *g-r* noise. This occurs because the thermal contribution to the *g-r* noise depends on the square root of the effective lifetime and the background contribution to the *g-r* noise depends linearly on the effective lifetime, [Eqns (6)-(8)]. As the recombination velocity is decreased,

both the thermal and background contributions to the *g-r* noise increase, but the background contribution increases at a faster rate[51].

As the thermally generated *g-r* noise contribution to the Ohmic contact detector (with $S_{srv} \rightarrow \infty$) is significant, the low frequency detectivity, D^*, is less than D^*_{BLIP} and D^* decreases with increasing field. Decreasing S_{srv} increases the responsivity and background-generated *g-r* noise faster than the thermal *g-r* noise and D^* becomes nearly equal to D^*_{BLIP} when the background-generated *g-r* noise dominates the thermal-generated contribution. At larger bias fields, it is necessary to go to smaller values of S_{srv} to reach this condition.

3.5 Surface Passivation Technology

Development of suitable passivation scheme is very crucial in fabrication of photoconductive arrays having uniform and high performance. The knowledge of interface and optimum interface properties in a particular situation is very essential for the development of a device. In addition to achieving the excellent interface properties, surface passivation technology also needs to be assessed in terms of uniformity and capability of producing multi-element arrays with minimum detector-to-detector variations in responsivity and specific detectivity. Several authors[103-109] have reviewed the surface passivation technology suitable for MCT material.

The passivant layer plays an important role in controlling the defects and providing physical, chemical, and electrical stability to the semiconductor surface. High densities of fixed charges and interface states are observed in the disordered surface region. Surface passivation controls the surface electrical properties of the semiconductor by reducing density of fixed charges and interface states, thus lowering down the surface recombination velocity. A good passivation should yield well-controlled, stable and spatially uniform interface electrical properties. It forms a chemically and physically protective layer over the active area of the device and shields it from environmental conditions. Passivation layer must have adequate physical, thermal, and chemical stability compatible with device processing. In front illuminated detectors, the optical properties of the passivant materials are of great importance. It must exhibit excellent transmission in the relevant spectral region. A good passivation should also exhibit radiation hardening to avoid degradation of the detectors in harsh environments, such as space, etc.

The *HgCdTe* surface passivation is complex because of the compound nature of the semiconductor, the difference in the chemical properties of the constituents, and also due to the tendency of electrically active defect formation in the interface region prior to and during passivation process. Defects movement from bulk to surface and vice versa, even at room temperature, is a severe problem. This is directly related to the weakly bound and highly mobile mercury atom. The *HgCdTe* surfaces cannot be exposed to temperatures above 80 °C, a limit imposed to control the loss of mercury due to weakness of mercury-bonding in the lattice and the properties of atomic mercury such as its low melting point and high vapor pressure[103]. The band gap of *HgCdTe* for LWIR is of the order of 100 meV, which is almost equal to surface band bending and it is very easy to accumulate, deplete, or invert the surface.

Passivants employed for the passivation of *HgCdTe* photoconductive detectors result in repulsion of photo-generated minority carriers from surface, thereby reducing surface recombination velocity-desirable effect. But at the same time, a passivant forms an accumulation layer of majority carriers which acts as a surface shunt resistance parallel to detector resistance–an undesirable effect. Pal,[110] *et al.* developed a model and shown that the optimum performance of a photoconductive detector is obtained for the values of fixed charge density, Q_f, and interface trap density, D_{it}, of the order of $5\text{-}10 \times 10^{10}$ cm^{-2} and 1×10^{10} cm^{-2}eV^{-1}, respectively. Hence, the requirements for a suitable passivant layer should be such that it provides passivation to the detector surface. This results in reduction of $1/f$ noise and preservation of bulk lifetime. Also, it encapsulates the MCT material, thus preventing its decomposition and protecting the device from external contamination.

The single most important mechanism that limits photoconductor performance is carrier recombination at the device surface, which effectively reduces

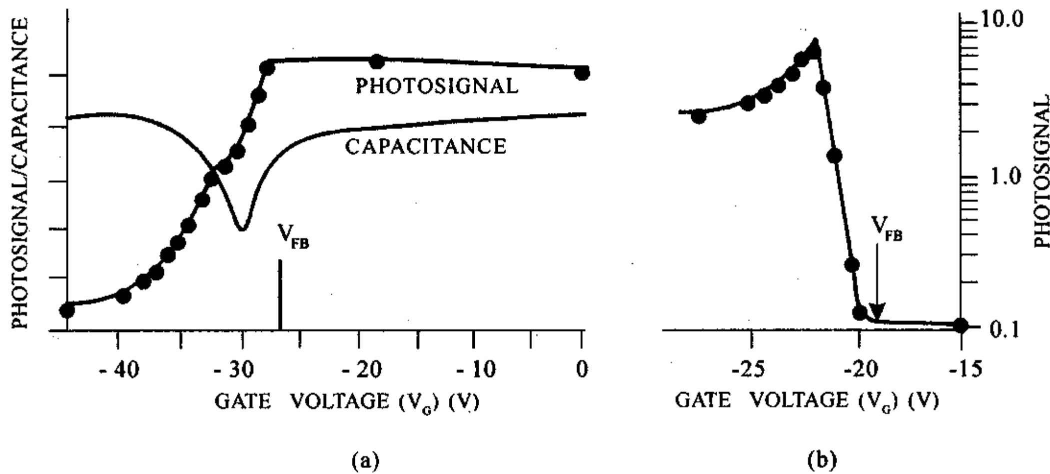

Figure 10. (a) Photosignal and capacitance versus gate voltage for 0.1 eV *n*-MCT photoconductor at 77 K and (b) photoconductivity signal versus gate voltage for 0.3 eV *n*-MCT photoconductor at 77 K.

the minority carrier lifetime. It is well known that the surfaces of a semiconductor are regions where recombination can proceed at a higher rate than in the bulk. Surface recombination reduces the total number of steady state excess carriers by effectively reducing the average recombination time. In fact, much of the technology of the present-day device fabrication aims at minimising surface recombination of minority carriers by appropriate chemical and mechanical surface preparation methods, and subsequently passivating the surface with a native or a deposited insulator film, or a combination of both[105].

It must, however, be pointed out that the surface potential can have a drastic influence on the bulk photoconductive lifetime even if no surface states are present[111]. This becomes obvious if one considers the dark current flowing in a surface region, which is under strong inversion. The electron-hole pairs generated by incident photon flux within the depletion region or within the diffusion length from it will be physically separated and will recombine at a rate determined by the response time (R_dC_d) of the depletion region. Under thermal equilibrium, this time constant will be controlled by the dominant dark current source as discussed earlier, that is, by the diffusion, depletion region, surface, or tunnel currents.

Surface-controlled photoconductivity has been demonstrated by Kinch[112] on a photoconductive element ~20 μm thick, using *n*-type $Hg_{1-x}Cd_xTe$ (E_g = 0.1eV) with a bulk lifetime of ~ 3 μs, with the upper surface completely controlled by a transparent field plate on a 1 μm layer of native oxide plus *ZnS*. This MIS structure has a flat-band voltage of –27 V. The photosignal and capacitance versus gate voltage for this sample are shown in Fig. 10(a). The photosignal is observed to be relatively flat in the region of surface accumulation. However, on changing the gate voltage from accumulation to depletion condition, the photosignal decreases dramatically, being reduced by more than an order of magnitude for a strongly inverted surface condition. A typical depletion region time constant (R_dC_d) for this material is 2×10^{-7}s at 77 K.

The higher signal in the accumulation condition is due to the effect of the built-in transverse electric field, which drives the minority carriers away from the surface towards the bulk, resulting in increased lifetime. The wider gap compositions of $Hg_{1-x}Cd_xTe$ at 77 K, on the other hand, can exhibit photosignal enhancement upon surface inversion, relative to the accumulation condition, as shown in Fig.10 (b), because the values of the depletion region time constant in this case are considerably in excess of the minority carrier lifetime, τ_p, which is typically[112] in the range $10^{-6} < \tau_p < 4 \times 10^{-5}$ s at 77 K.

The effect of the surface recombination on the performance of a photoconductive detector was investigated theoretically by Broudy[46] as shown

in Fig. 11 for *n*-type $Hg_{0.8}Cd_{0.2}Te$ (λ_c = 14.2 μm at 80 K) with a net carrier concentration of 9×10^{14} cm^{-3}. Compared with an ideal photoconductive detector,

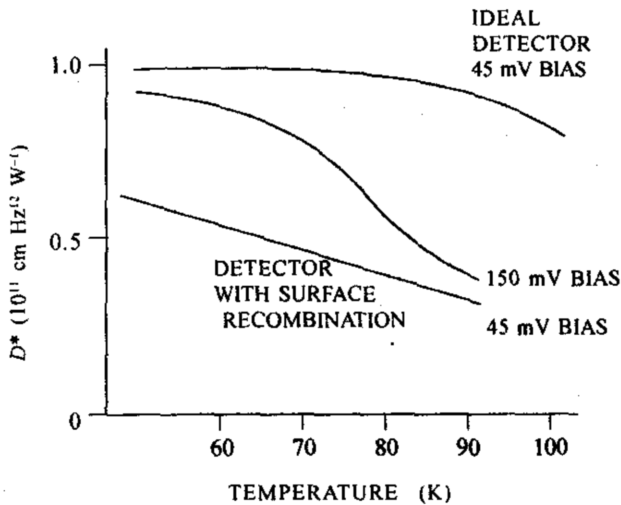

Figure 11. Theoretical detectivity as a function of temperature. Ideal case (upper curve) at 45 mV for zero surface recombination velocity, no sweep-out and ideal thermal interface. With added surface recombination velocity, sweep-out and a thermal interface at 45 mV bias (lower curve) and at 150 mV bias (middle curve).

with its front and back surfaces having zero surface recombination velocity, the detector with surface recombination was assumed to have its back surface with infinite recombination velocity. It can be seen that the addition of surface recombination considerably reduces the detectivity. The performance of the ideal detector properties for temperatures above 80 K as thermally generated minority carriers begin to dominate.

Transverse electric field on the surface of a photoconductive detector is commonly used to reduce surface recombination. In this approach, the minority carriers are prevented from reaching the surface by means of a built-in electric field. For example, for an *n*-type MCT photoconductor, a transverse field would be provided by a n^+ accumulation layer induced on the surface of the semiconductor by a positive fixed charge present in the anodic oxide passivation layer. Implantation or ion milling can also be used to create *a* n^+ layer on *n*-type MCT surfaces providing Hi-Lo n^+- *n* junction, which sets a reflecting barrier for minority carriers. It may be noted here that the same principle of high-low junction is used for reflecting the minority carriers at the contacts of these detectors, thus increasing their lifetime and also reducing the sweep-out effects.

The effect of fixed charge density (Q_f) of the passivant on the performance parameters of *HgCdTe* photoconductive extended/overlap structures was investigated theoretically by Bhan[113], *et al.* extending Smith model[83,84] by including the effect of passivation for a detector with pixel size 35 x 50 μm^2, thickness 10 μm, x = 0.21 and $n = 5 \times 10^{14}$ cm^{-3}. Their results show that the responsivity dependence on Q_f shows a peak for both symmetric as well asymmetric overlap structures for the optimised Q_f value of ~2-3 × 10^{11} cm^{-2}. The noise shows almost no dependence on Q_f for lower values up to ~ 1 × 10^{11} cm^{-2}, decreases sharply for values > 4 × 10^{11} cm^{-2} and shows a peak at intermediate value ~3 × 10^{11} cm^{-2}. Q_f ~ 2 × 10^{11} cm^{-2} is found to be optimum for maximising D^* for both the standard and the overlap structures. However, there is a stronger dependence on Q_f of the detector parameters for overlap structures than for standard structures.

4. DEVICE PROCESSING TECHNOLOGY

The photoconductive detectors can be fabricated by the methods, many are quite similar to the processes used in *Si*-ICs, such as lithography, etching, insulator deposition, vacuum metallisation, bonding, etc. Additionally, some MCT specific techniques such as slab mounting on sapphire, thinning by lapping and polishing, MCT array structure etching, etc. also have to be applied. As discussed earlier, the MCT has weak *Hg-Te* bond and mercury has low vapour pressure, therefore all the processing steps have to be optimised at or below 70 °C and active area should never be exposed to chemical etchants. The presence of a 10 μm MCT step on sapphire introduces a non-planarity in the process due to which the processing becomes critical, particularly the lift-off metal patterning. The actual photoconductive $Hg_{1-x}Cd_xTe$ sensor used in IR systems is a complex multi-element array requiring a high level of sophistication in analysis, design, and processing.

State-of-the-art processing of MCT detectors must be capable of achieving the following key requirements:

- Bulk MCT crystal properties throughout fabrication process must be preserved.
- All surfaces must be damage-free and well passivated.
- Ohmic/blocking contacts of proper geometric configuration must be provided.
- Detector's active area must be defined accurately.
- Material thickness must be controlled to close tolerances.

Major process steps normally used in the fabrication of a photoconductive array[46,114,115] are shown in Fig. 12 in the form of a flow chart. Details of some critical and important processing steps/issues are described below.

4.1 Substrates Selection

The choice of substrate material is governed by physical and optical characteristics, such as thermal expansion, inertness, fragility, reflective index, conduction as well as availability and cost. The critical issues are flatness, parallelism, and surface finish. To maintain dimensional control of the finished device, it is necessary to properly specify the substrate to which the device will be attached. The most favoured substrate is sapphire because of its physical, optical, mechanical, and electrical properties. It has high thermal conductivity and very low electrical conductivity. It is chemically inert and can be polished to achieve high surface flatness and plane-parallelism of the two faces within the tight tolerance of ~1 μm.

4.2 Sample Preparation

Lot of efforts have been made to prepare damage-free MCT surface. This involves successive removal of surface damage by lapping and polishing with finer abrasive grit sizes, followed by chemo-mechanical polishing. Lapping is carried out at low pressure and low speed. A precision lapping and polishing machine, such as Logitech PM2A and PM5 machines can be used for this purpose. Surface is checked for grain boundaries. Wafer thickness is monitored at each stage of polishing.

Polishing is a high load process compared to lapping and is carried out at higher speeds. The principal advantage of chemical polishing over mechanical polishing lies in the fact that it reduces sub-surface damage to the crystal structure. In mechanical lapping and polishing, fine scratches are introduced in the material which are associated with dislocations and deformation of the material. The damaged region typically comprises: (i) a surface layer of amorphised semiconductor and embedded abrasive (Billby layer), (ii) a polycrystalline zone, and (iii) a dislocated zone extending deep into the sample[116].

Sharma,[116] *et al.* have presented a detailed study on the effect of damages generated in MCT material during surface preparation on lifetime of excess carriers. The lifetime measurements were done using microwave reflectance technique. The depth of damaged region keeps on reducing with polishing powder grit size, which leads to corresponding improvement in lifetime. The polishing damage of the previous stage is removed in the next stage of polishing These defects are estimated to a depth of approx. 20 times the grit size[117], therefore, care should be taken to remove the material, at least up to this depth, while using lower grit polishing powder.

Prepared MCT surface is characterised using ellipsometry. Rhiger[118] has used ellipsometric measurements to characterise the MCT surface after it has been subjected to various surface treatments. Bromine-methanol etchant leaves the surface tellurium-rich. Dilute HNO_3 treatment is used to remove this excess tellurium-rich layer.

The MCT slabs of required size are cut after the wafers are backside passivated. Sapphire substrates (of required thickness uniformity) are thoroughly cleaned using standard cleaning procedures. Generally, a low-temperature epoxy is used for bonding MCT

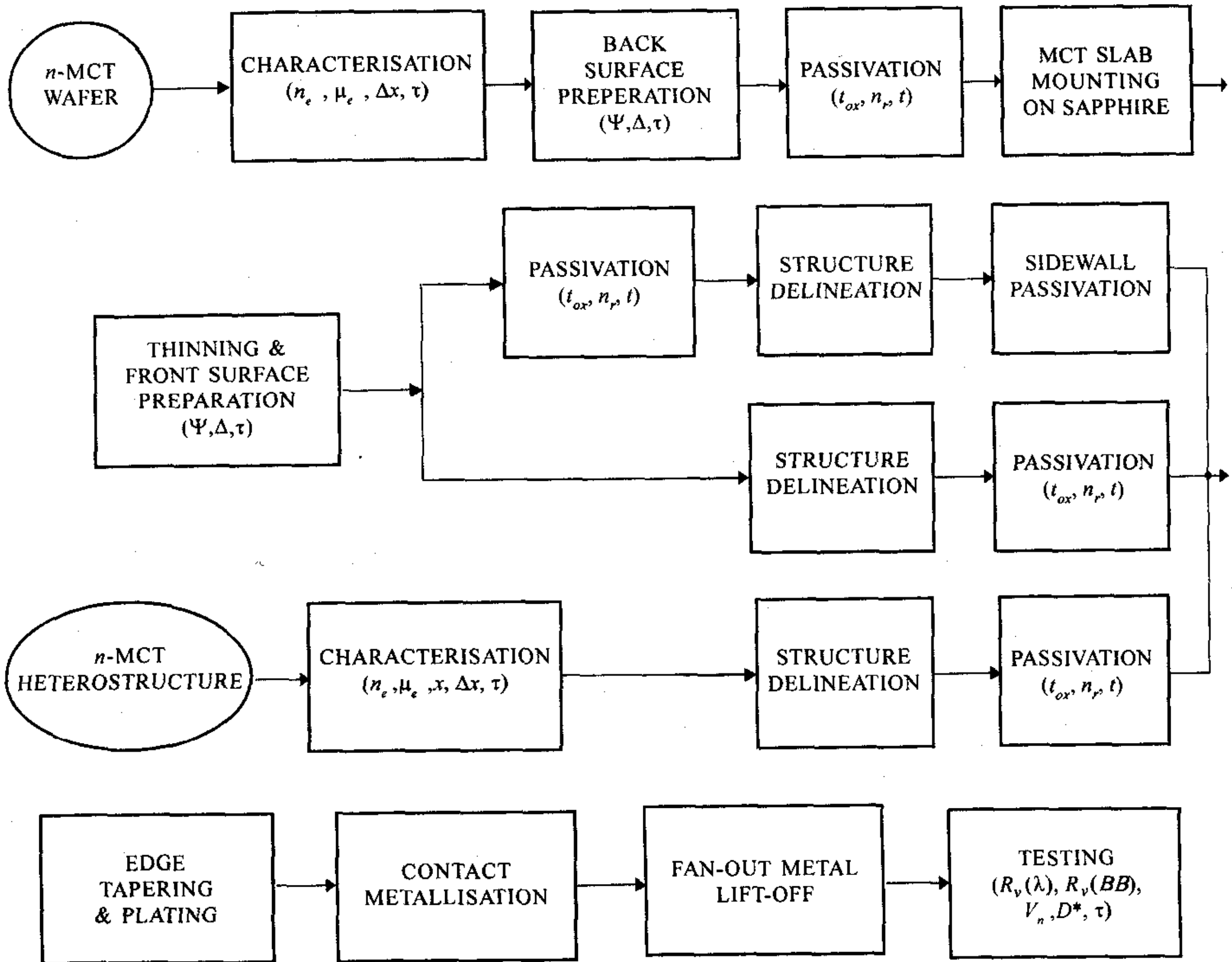

Figure 12. Major process steps used in the fabrication of a photoconductive array. Starting with bulk-grown wafers, the process after front surface preparation may follow either of the two paths: (i) surface passivation first, followed by detector structural delineation or (ii) structural delineation first, followed by surface passivation. Starting with epitaxial wafers, the process gets simplified with no material thinning required.

slabs with sapphire using special epoxy mounting fixtures. Bonding material has two components comprising resin and hardener that are mixed in the specified ratio and diluted with organic solvent to get a thin uniform layer. Epoxy curing is done at temperatures lower than 70 °C. Front surface preparation is carried out in a way similar to back surface preparation, leaving final MCT thickness ~ 10 μm. Prepared surface is characterised using optical microscope, ellipsometer and scanning electron microscope. It is to be pointed here that the photoconductive detectors are also fabricated using infrared absorbing epitaxial layer of *n*-type $Hg_{1-x}Cd_xTe$ of appropriate thickness on insulating substrate[99], such as *CdTe/CdZnTe*. The process of sample preparation is considerably simplified using *epi* layers and the above laborious steps of lapping and polishing are totally avoided.

4.3 Surface Passivation

The semiconductor-passivant interface as well as the dielectric properties of the passivating layer play important and often dominant role in determining device performance. Passivation technologies can be classified into three categories: (i) native films

(oxides, sulphides, fluorides), (ii) deposited films (ZnS, SiO_2, Si_3N_4, polymers), and (iii) in-situ grown heterostructures where wide band gap layer acts as passivant. A native layer, which becomes an integral part of the semiconductor, is formed when the growing layer incorporates the semiconductor atoms. Thick native films become porous and do not adhere well to the substrate. Therefore, thick deposited dielectric films like ZnS are required for passivation to achieve the protection of the interface from environmental conditions by acting as a protective coating. These deposited films are required to insulate the metallisation pattern of the contacts and the bonding pads from the substrate. Thus, these films must be mechanically stable, electrically insulating, free of traps, transparent in the relevant wavelength region, and chemically protective.

Since all surfaces must terminate with damage-free passivation, the back surface, i.e., the surface to be epoxied to the substrate, must be passivated. The prepared MCT surface is passivated (to provide environmental protection, control surface leakage currents, and stabilise MCT chemically) using either native oxide, plasma oxide[15], or *CdTe*. Anodic oxide[103,119-123] is grown on MCT in an electrolyte of 0.1M *KOH* in 90 per cent ethylene glycol (EG) and 10 per cent deionised water in an anodisation cell.

The MCT wafers serve as the anode and growth is carried out at a constant current density 100-300 μA/cm² followed by a constant voltage anneal. The relationship of anodic oxide film thickness and applied voltage for anodisation at constant current density 300 μA/cm² is shown[119] in Fig. 13. The thickness and refractive indices of anodic oxide and the MCT surfaces are characterised using ellipsometer. For anodic oxides on MCT grown at constant current density 200 μA/cm², moderate fixed positive charge (5-7 × 10^{11} cm^{-2}) and small hysteresis are reported, achieving virtually an ideal condition for photoconduction[124].

Gauthier[125] patented a process for passivation of $Hg_{1-x}Cd_xTe$ (x = 0.2 or 0.3) photoconductive detectors, wherein a native oxide layer is formed by chemical reaction. The native oxide layer is

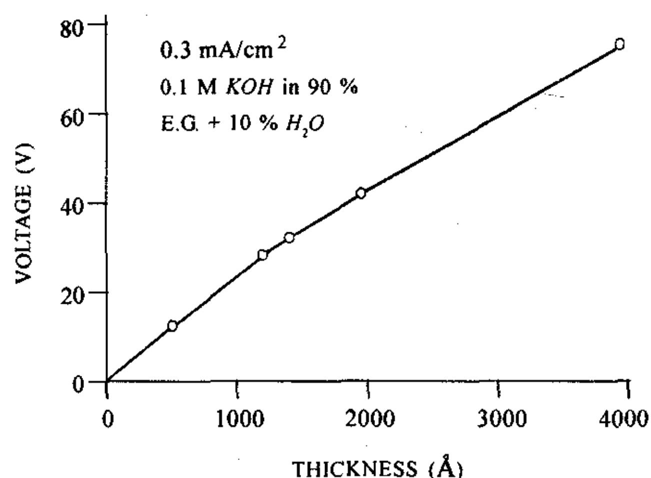

Figure 13. Variation of anodic oxide thickness as a function of anodization cell voltage for constant current anodization of $Hg_{1-x}Cd_xTe$.

made to grow by pure chemical oxidation in an aqueous solution of $K_3Fe(CN)_6$ (0.075-0.75 mole/l) and *KOH* (0.06-0.6 mole/l). The $Fe(CN)_6^{-3}$ ions react with *tellurium* of MCT to form TeO_2. The speed of oxidation depends on the concentrations retained in the solution and thickness of the oxide layer at any instant, i.e., as the layer thickness increases the speed of growth decreases as shown in Fig.14. Thus, a layer of 40 nm grows in the first five minutes and only 30 nm is added in the next 40 min. The passivant oxide layer is capped with complimentary ZnS layer of thickness 300-500 nm. The passivated detector obtained using these oxides is endowed with good characteristics, with stability up to 80 °C.

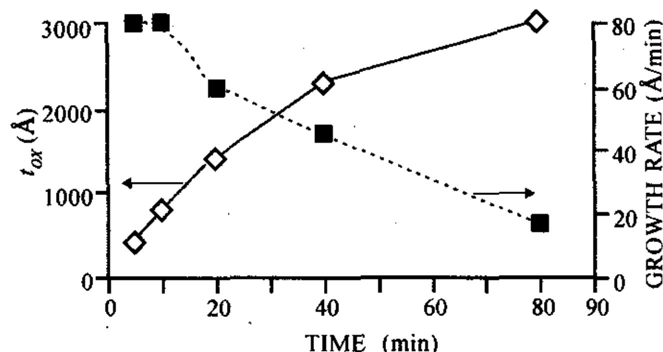

Figure 14. Variation of chemical oxide thickness and growth rate as a function of deposition time (Data taken from Ref. 125).

Table 4. Passivants producing positive fixed charges at the passivant/*n-HgCdTe* surface

Passivant	Passivant charge density Q_{ss} (cm^{-2})	Interface trap density D_{it} (cm^{-2} eV^{-1})	Adhesion	Insulator	Refrective index	Dielectric constant	Thermal stability limit (°C)	Chemical corrosion
				Native films				
Anodic oxide	2×10^{12}	3×10^{10}	Excellent	Inferior to SiO_2	2.1	19.3	70	Attacked by alkalis
Plasma oxide	1×10^{11}	2×10^{11}	--	Inferior to A.O.	--	--	90	--
Anodic Fluoride	2×10^{10}	--	--	Inferior to SiO_2	--	--	105	--
Chemical oxide	Detectivity (at λ_p = 4.5 μm and 195 K) > 10^{11} cm $Hz^{1/2}$ W^{-1}						80	--
				Deposited films				
CdTe	5×10^{10}	$< 1 \times 10^{10}$	--	-	--	--	--	--

The *CdTe* is generally deposited by thermal evaporation technique. Adequate precautions are taken to avoid heating of *HgCdTe* surface during evaporation. The evaporation rate of *CdTe*, chamber vacuum at the time of evaporation, substrate temperature, source-to-substrate distance, etc. are the crucial parameters, which need to be optimised to achieve a good *CdTe* layer.

A detailed comparison of different passivants used for PC devices[105,110] is given in Table 4.

Usually a photoconductive linear array consists of a number of detector elements (such as 60, 120, 180, etc.) in a row, which are further subdivided into combs–each containing 5–10 elements, as depicted in Fig. 15(a). After the front surface passivation, Br_2-*HBr* solution wet etching or ion-beam milling does the structural delineation of the MCT slab into individual combs with detector elements. This process of passivation prior to structuring has the inherent advantage of starting with a damage-free clean native MCT surface, which is well sealed by the passivant immediately after the surface preparation. However, during the process of etching, the sidewalls of elements are rendered bare and unpassivated. If left under these conditions, these unpassivated sidewalls will add to the detector noise and adversely affect the performance[115]. To overcome this problem, the chemical oxide growth process can be advantageously utilised for passivation of sidewalls of each element. The completed device is dipped into chemical oxide growth solution of $K_3Fe(CN)_6$ and *KOH* allowing the chemical oxide to grow selectively on the exposed MCT sidewalls, as described earlier[125]. However, the chemical oxide is relatively

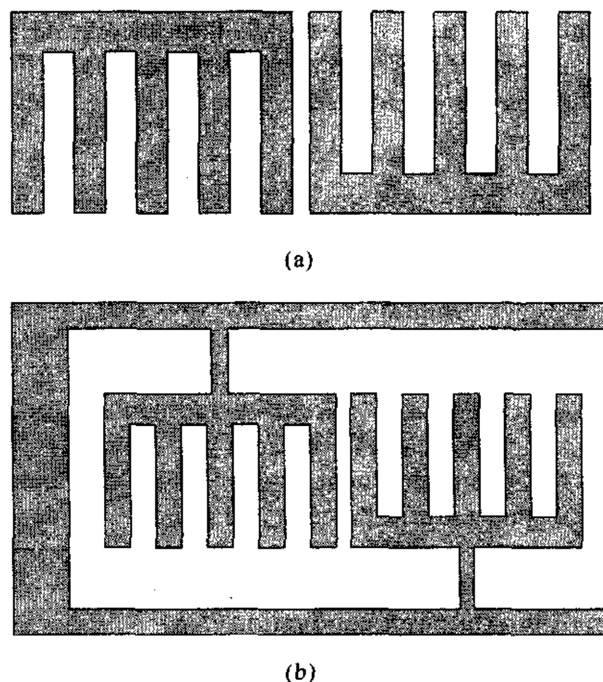

Figure 15. Schematic diagram of the part of a $Hg_{1-x}Cd_xTe$ linear array depicting two combs each having five elements for: (a) delineation after passivation and (b) passivation after delineation.

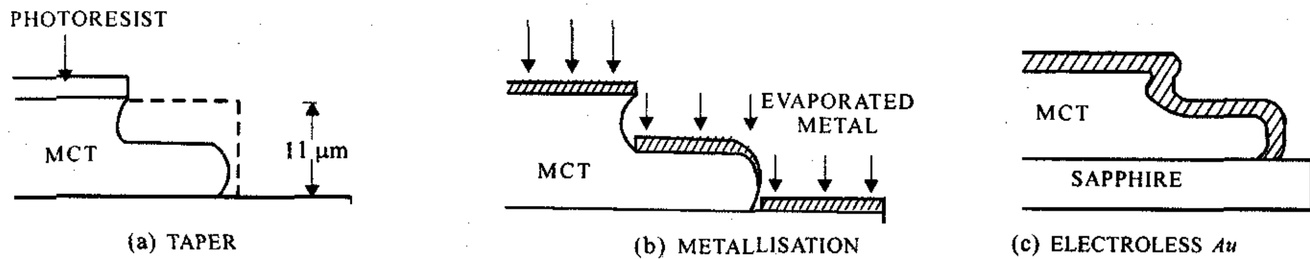

Figure 16. (a) Taper etch profile, (b) improper metal step coverage leading to uncertainty in metal continuity and unstable detector resistances, and (c) electroless *Au* deposited on tapered edge, covering all the surface with metal.

inferior to anodic oxide in passivating properties. After this step, the MCT surface is covered by either passivant or metal layer. This results in an improvement in the detector's figures of merit.

An alternate structural delineation approach would be to etch or ion mill individual elements into the MCT slab prior to front surface passivation by keeping a common corridor of semiconductor for electrical continuity, as shown in Fig. 15(b). This is followed by anodic oxide growth. Subsequently the common corridor is etched off, leaving desired comb structure with all surfaces passivated by anodic oxide in a single step.

This method, however, suffers from the disadvantage that after completing the delineation the exposed surface could be laden with some uncontrolled growth of oxides or other chemical remnant left on the MCT surface. These oxides and residues are extremely hard to be removed. Also, it is found that the anodic oxide growth solution attacks exposed epoxy under the structure during the growth. Several workers have tried different chemical treatments to obtain the nascent clean MCT surface. For example, light spray-etch with one sixteenth per cent bromine solution in ethylene glycol is applied, followed by solvent cleaning process in toluene, acetone, methanol, and isopropanol sequentially sprayed[126].

In an alternate approach of array fabrication, using infrared absorbing epitaxial layer of *n*-type $Hg_{1-x}Cd_xTe$, the surface is automatically passivated in situ in the epitaxial chamber by further growing higher x (0.24) material[99], followed by *ZnS* protective capping. This higher x layer creates a heterostructure barrier needed for blocking contacts for high performance detectors[85].

4.4 Metal Step Coverage

The complexity of device processing arises due to non-planarity of the device. It has a 10 μm steep MCT step, which is tapered at the ends–a step essential for continuous metal coverage. For reliable and repeatable functioning of device, the metallisation must be continuous over the *HgCdTe* and epoxy edges onto the substrate surface. However, even minor overetching during tapering may lead to improper metal step coverage on the 10 μm steep MCT edge and run-over to the sapphire leads to uncertainty in metal continuity and causing flicker in the element resistances [Fig.16]. This requires optimal control on MCT edge profile etching, i.e., proper rounding. This can be done by optimising the distance of the tapered edge from the device edge, the dilution of etchant (bromine ratio in *HBr*) and etch time.

The metallisation of such steps with reliable and reproducible metal step coverage usually requires complex rotating mechanisms and jigs in a thermal evaporation system. While the requirement for successful lift-off process is that the deposition should be normal to the surface, which is not possible with the above-mentioned systems. In addition, exposure of tapered area to the atmosphere before metallisation leads to uncontrolled growth of oxide. However, both of these problems can be solved by a much simpler in-situ electroless gold deposition technique using auric chloride solution[127]. After achieving rounded MCT taper edge by etching, the gold solution is applied on the exposed edge, which leaves the surface covered by gold due to higher affinity of the MCT for gold. This process eliminates the metal continuity failures drastically and reduces element resistance variations.

4.5 Hi-Lo Blocking Contacts Area Milling

The need of freshly cleaned semiconductor surface prior to metallisation to achieve low-contact resistance was realised earlier[101]. The use of chemical etching for this purpose sometimes leads to undesired complex formation, such as uncontrolled oxide growth on the semiconductor surface–an unreliable process. On the other hand, ion-beam milling is a novel etch technique, which is anisotropic, non-selective, and highly reproducible. Also, as discussed earlier, the main advantage of ion-beam milling is desirable modification of electrical properties of semiconductor in contact region from n-or p-type to n^+-type[90-95].

The depth of converted region depends on ion current density. Figure 17 shows profiles of carrier concentration versus etch depth at various ion current densities, for a fixed ion etch time of 15 min. At very low ion current density, i.e., 0.3 mA/cm^2, the etch rate of *HgCdTe* is almost zero and increase in carrier concentration is approximately two times its original value. As the ion current density is increased to 0.34 mA/cm^2, the etch rate is ~ 13 nm/min and increase in carrier concentration is of more than three order over its original value. Further increase in the ion current density results in increase in carrier concentration and also the depth of converted region. At the ion current density of 0.6 mA/cm^2,

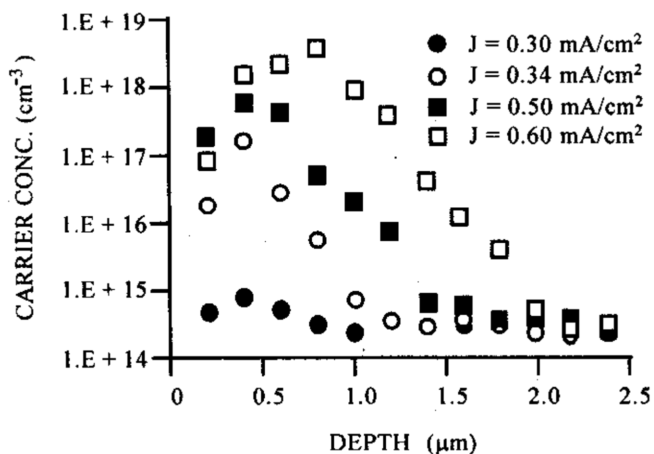

Figure 17. Carrier concentration depth profiles at various ion current densities. Etch removal of the amorphised top material layer up to the depth of the peak of the carrier concentration prior to contact matellisation leads to improved contacts.

the etch rate is 270 nm/min and increase in carrier concentration is of more than four order. At ion current density of 0.6 mA/cm^2, it is observed that *HgCdTe* sample surface has been damaged, as viewed optically. Also, the carrier concentration is low at the surface[95].

The exposure of photoresist to ion milling is inevitable during device processing; hence, the processing conditions as photoresist treatment and ion energies play a very crucial role for success of the step. During ion bombardment, photoresist gets hardened and is very difficult to remove after the process is complete. Generally, the methods commonly used for removing this hardened photoresist in silicon technology are not suitable for MCT, because of involvement of high temperatures and/ or stark action of strong chemicals. Mittal[128], *et al.* have studied effects of various alternative treatments to photoresist prior to ion bombardment. UV hardening after the development of the photoresist pattern hardens the developed photoresist. The aim is to harden the photoresist prior to exposure to ion bombardment, so that the further hardening during ion milling can be slowed and the removal of photoresist in hot acetone spray is possible.

The ion bombardment adversely affects the lip structure of photoresist, required for lift-off process. Bhan[129], *et al.* have studied the effect of ion current density on the desired shape/profile of lip structure formed in photoresist prior to actual lift-off. At lower ion current densities up to 0.5 mA/cm^2, virtually no adverse effect on the lip structure is observed, while at higher current densities (0.7 mA/cm^2) the lip structure is significantly damaged (Fig. 18) leading to lift-off failure.

4.6 Fan-out Metallisation

No semiconductor device can function without any electrical contact to outside world. The various metallisation schemes used for this purpose have to be suitably patterned. This can be done either by selective chemical etching after the complete metallisation or by lift-off process. The stark chemicals used in wet etching adversely affect anodic oxide passivant and *ZnS* capping layer which are porous, and hence, susceptible to chemical seepage and

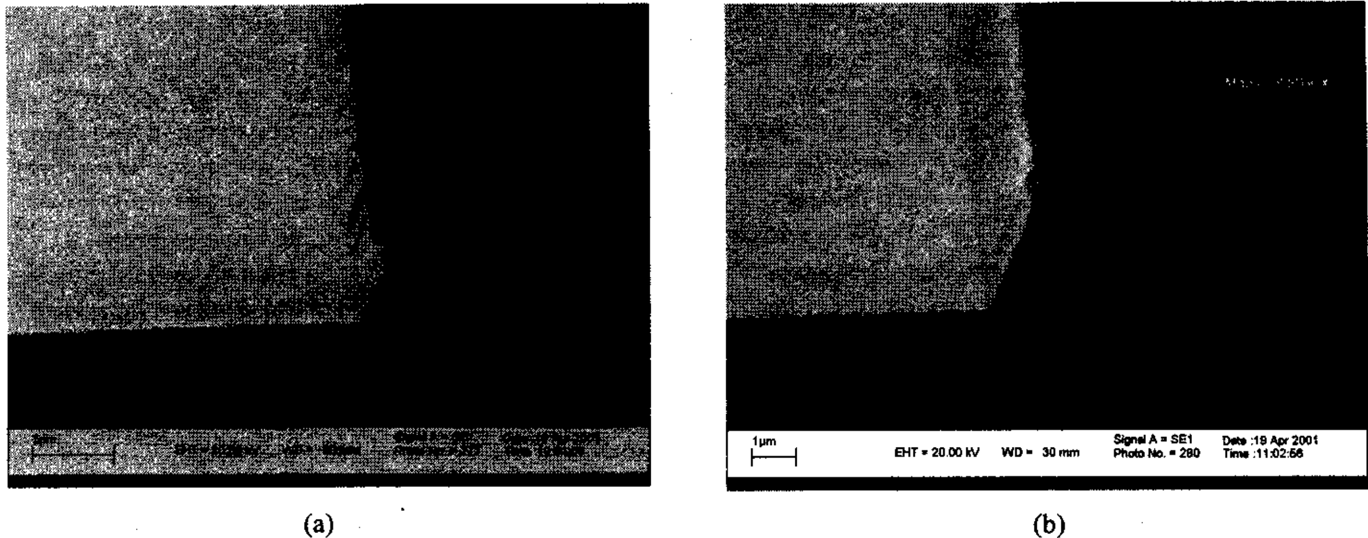

Figure 18. Cross-sectional SEM micrographs of the photoresist lip structure: (a) milling at current density 0.34 mA/cm²–a desired profile and (b) at 0.70 mA/cm²–the lip structure shrinkage due to damage.

unwanted reactions. The etching process at this stage is, therefore, ruled out. The advantages of lift-off process over selective etching have been discussed[130,131]. For lift-off process, conventional photolithographic step is modified slightly by soaking in chlorobenzene after exposure and prior to the development of pattern. This soaking modifies the photoresist profile near the edges to mushroom-type having negative slope, which helps in lift-off process.

Device yield depends considerably on the success of the metal fan-out pattern lift-off. This process involves preparing a proper photoresist hangover lip structure using chlorobenzene-soak treatment before normal incidence metal evaporation. This step becomes very critical because of highly non-planarity of the device topology, leading to photoresist thickness variation on the detector fingers. For achieving a proper hangover lip structure, all photolithographic parameters like pre-bake time, chlorobenzene-soak time, UV radiation dose, etc. are to be standardised.

5. DETECTOR CHARACTERISATION

The equipment used to measure the necessary detector parameters and the test procedures are well documented in the literature[13,132,133]. A measurement setup consists of an electronic equipment, a blackbody source, a variable frequency source, a monochromator source, a reference detector, a test dewar, and a variable voltage supply for biasing detector. The electronics normally used consists of a preamplifier, an amplifier, a spectrum analyser, and calibration instruments. The responsivity measurement requires a stable, modulated source of infrared radiation at three frequencies up to 1000 Hz to measure detector signal dependence on modulation frequency.

In routine practice, the test laboratories operate blackbody temperature at 500 K and the radiation is modulated by chopping at 800 Hz. The test setup for measurements of spectral responsivity basically remains the same except that the blackbody source is replaced by a monochromator. Radiation of a specified wavelength, range from the monochromatic source is allowed to fall on the detector and photosignals so generated are recorded. As the thermal detectors exhibit a flat spectral response, the generated thermosignals will be proportional to the incident monochromatic power. The ratio of photosignal to thermopower when plotted against the wavelength yields the relative spectral response curve normalised to peak response. Peak response wavelength (λ_p) and cutoff wavelength (λ_c) are obtained from this curve. At cutoff wavelength, the response drops to 50 per cent of its peak value towards the longer wavelength. The rms noise voltage of a detector is measured by the lock-in amplifier generally at 20 kHz central frequency with a 10 per cent equivalent

noise bandwidth (ENBW), when chopper is off and blackbody aperture is closed. Normally, the measured noise mainly represents the *g-r* noise, as all other noises become negligible. Johnson noise is very small for low- resistance devices at cryogenic temperatures; $1/f$ noise becomes negligible at 20 kHz; V_a is also kept very low by selecting a low noise amplifier and good laboratory techniques of grounding, shielding, etc. Frequency-dependent behaviour of the noise components is estimated by measuring the rms noise voltages at various frequencies in the 0.1–100 kHz.

In military applications, the MCT infrared detectors are operated at cryogenic temperatures to enhance their performance. For this purpose, the detectors are encapsulated in miniature/tactical glass or glass-to-metal dewars. Joule-Thomson cryocoolers, capable of cooling detectors to operating temperatures 80-90 K in a few seconds are in use in seeker/guidance systems. Thermoelectric and stirling cycle cryocoolers are also used in a variety of night vision, targeting and guidance applications, in both the ground-based and airborne systems[134].

6. TECHNOLOGY ILLUSTRATIONS

As cited above, tremendous amount of work has been done in the last couple of decades in the field of *HgCdTe* photoconductive detector technology and it is almost out of place to cover these studies even briefly and do any semblance of justice to it. It was, therefore, thought to be appropriate to discuss only a few selective studies that are in a way representative of the developments in the field at different stages and have bearing on the theme of topics covered.

Borrello[135], *et al.* have calculated the variations in vital detector parameters with background photon flux, ϕ_B and validated their model by observing excellent agreement with experimental data. The photoconductive lifetime, τ, is limited by Auger recombination at 77 K for flux $\phi_B > 10^{16}$ photons cm^{-2}s^{-1}. As the lifetime recovers with decrease in FOV from 180° to 30°, the response time in excess of 2 µs becomes observable. In correspondence with the lifetime, the responsivity increases significantly with reduction in FOV. It is, therefore, advantageous for a system designer to keep FOV smaller in the practical FOV range of 180° > FOV > 30°. At low background, *g-r* noise varies as $\phi_B^{1/2}$ reflecting decrease in minority carrier density and constant n and τ. At high background, *g-r* noise varies as $\phi_B^{-1/3}$. However, for the practical range of FOV (180° >FOV> 30°), the *g-r* noise remains practically constant. Excess $1/f$ noise is seen to be correlated to minority carrier density. $1/f$ noise corner frequency decreases for reduced FOV. D^* values for the cases $n>>p$ and $n = p$ have been estimated. In general, D^* increases with reduction in FOV, as shown in Fig. 19.

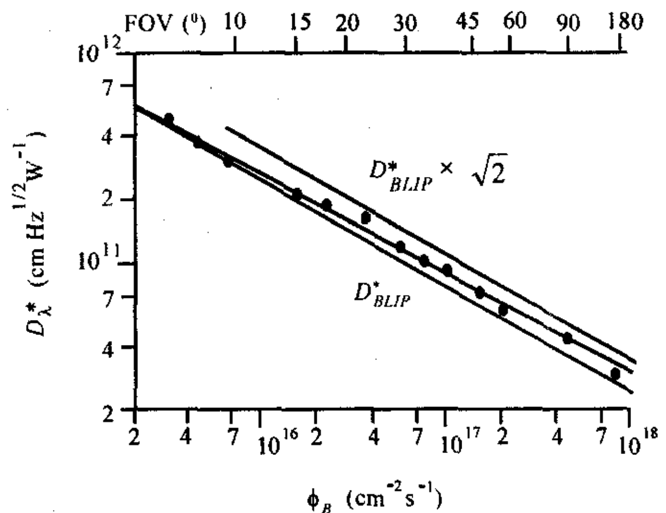

Figure 19. Peak D^*_{BLIP} versus background flux for $Hg_{1-x}Cd_xTe$ ($x = 0.1$ eV) photoconductive detector when $n >> p$. Upper limit is $D^*_{BLIP} \times \sqrt{2}$ when $n = p$. Experimental data points follow calculated D^* values for $n_0 = 6 \times 10^{14}$ cm^{-3}, assuming $\eta = 0.6$.

The temperature variations of D^*_λ, R_v, and *g-r* noise over the range 64–190 K were predicted theoretically for the thermally limited case for *n*-type photoconductor[62] with $n_0 \approx 8 \times 10^{14}$ cm^{-3} and $\lambda_{co} = 12.5$ µm. The temperature variations of D^*_λ predicted theoretically and measured experimentally are illustrated in Fig. 20 (a). The measured D^*_λ values of well over 10^{12} cm Hz$^{1/2}$ W^{-1} in the nitrogen temperature range were obtained. The FOV used in these measurements are estimated to be ~ 3° using $\eta = 0.6$ and $\lambda_{co} = 12.5$ µm. The temperature dependence of R_v is contained in the factor τ/n_0

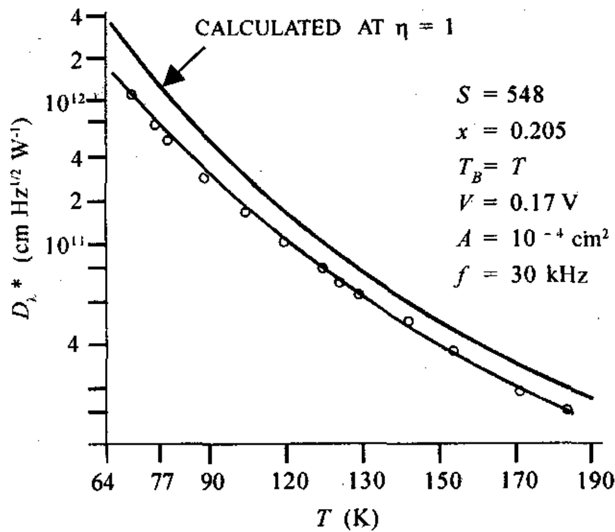

Figure 20(a). Temprature variation of measured and calculated detectivity.

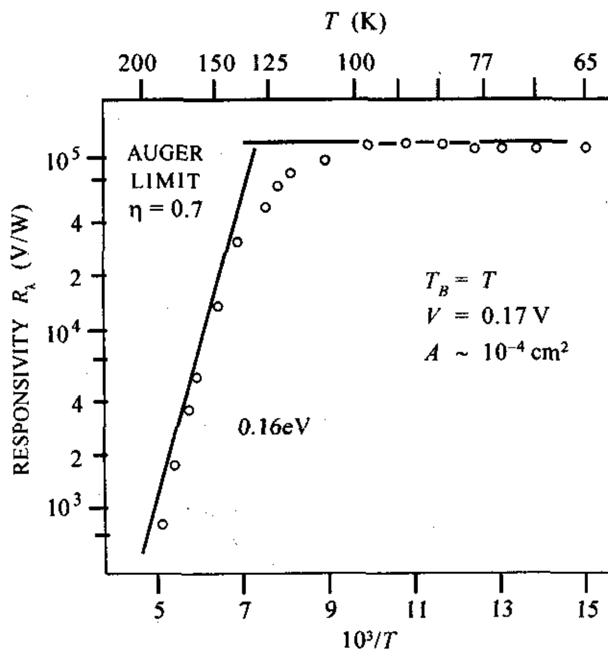

Figure 20(b). Temprature variation of measured and calculated responsivity for intrinsic regime.

and is given in Fig. 20 (b), showing an excellent agreement between theory and experiment. The R_v is virtually independent of temperature below 100 K and has a slope of 0.16 eV in the intrinsic range. The temperature dependence of *g-r* noise, V_{g-r}, set by the factor $(T_{Ai} / n_i)^{1/2}$, is shown in Fig. 20 (c). The calculated solid lines for the intrinsic and extrinsic cases are in perfect agreement with the experimental plot of points. The 1/*f* noise does

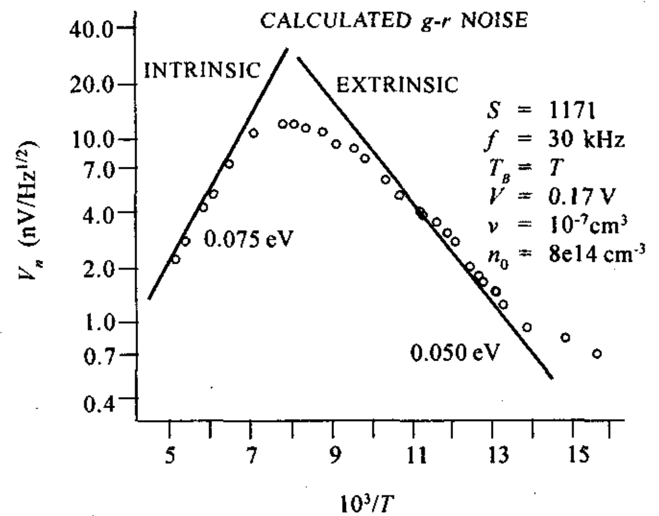

Figure 20(c). Temprature variation of measured noise at 30 kHz and calculated thermal noise.

not exhibit any strong dependence on the temperature, suggesting that 1/*f* noise is not due to thermally generated carriers but possibly is a majority carrier phenomena.

The advantage of a totally asymmetric overlap structure is illustrated in Fig. 21 showing the blackbody responsivity dependence on electric field of one of the 60 elements of an *n*-type photoconductive linear array with $x = 0.208$, $n_o = 4 \times 10^{14}$ cm^{-3} and pixel size[136] of 34 μm × 48 μm . Although the resistance of the detector remains the same in two directions of the field polarity, the overlap advantage is obtained with the detector finger as cathode and

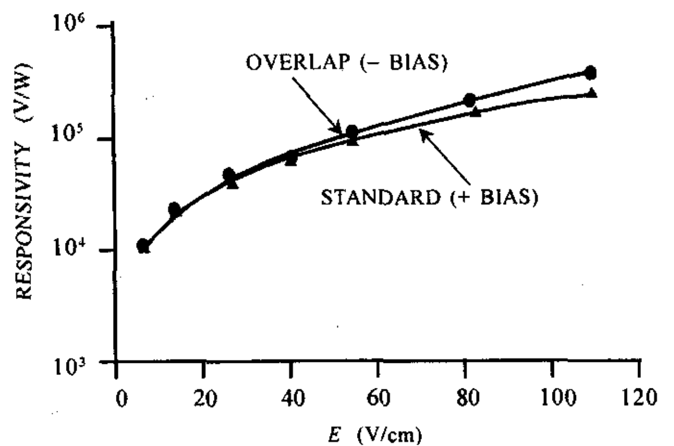

Figure 21. Responsivity versus electric field for standard and overlap structures of one of the 60 elements of an array.

the common contact of the comb having five elements as anode and, therefore, power remains the same for both the polarities. The responsivity is higher by a factor of 1.5 at 100 V/cm for the overlap compared to standard mode of operation. Also, the responsivity keeps on increasing almost linearly even at higher fields with no sign of saturation, as expected of such a structure.

Figure 22 shows the responsivity and detectivity versus field at 80 K for a symmetric heterostructure contact photoconductor (HCP) device[51] fabricated on a lightly doped $Hg_{1-x}Cd_xTe$ double layer LPE wafer with a compositional difference $\Delta x = 0.03$ between the lower active region ($n \sim 2 \times 10^{14}$ cm^{-3} and $\lambda_{co} = 7.88$ µm) and top higher bandgap blocking layer. It can be noticed that there is no sweep-out effect at the typical fields and responsivity values in excess of 1×10^6 V/W were measured on the device. The saturation sets in only for fields ~140V/cm. Comparatively, for the device with single layer ($\Delta x = 0$) with similar material parameters, the responsivity is one order lower and the saturation sets in at lower fields ~ 80 V/cm. The detectivity for the HCP detector remains constant at low-bias fields (7-8 x 10^{10} cm Hz$^{1/2}$ W^{-1}) and starts to decrease at fields > 100 V/cm. This type of behaviour in D^*_λ mechanism is consistent with *g-r* noise, where the thermal and background contributions to the noise are matching.

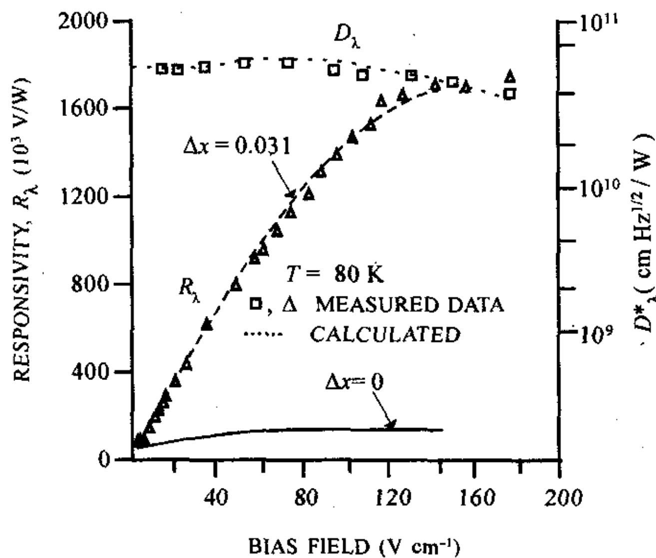

Figure 22. Responsivity and detectivity versus bias field for standard ($\Delta x = 0$) and symmetric heterostructure ($\Delta x = 0.031$) contact photoconductor.

Blackburn[44], *et al.* realised high performance 8-element SPRITE detectors in production using $Hg_{1-x}Cd_xTe$ wafers with $x = 0.21$, lifetime of 2 µs, ambipolar mobility 390 cm^{2}v^{-1}s^{-1} for 8-14 µm band. Standard SPRITE device consists of an array of 8 in-line elements. Each element is 700 µm long and 62.5 µm wide on a 75 µm pitch. Readout bifurcated contacts have been brought out parallel to the length of the element. The mean values of D^*(500 K, 20 kHz, 1, 62.5 × 62.5 µm^2) = 1.1×10^{11} cm Hz$^{1/2}$W^{-1} and responsivity = 6.0×10^4 V/W were achieved. The performance variation of such a SPRITE detector (λ_{co}=11.5 µm) with bias field and FOV is shown in Fig. 23.

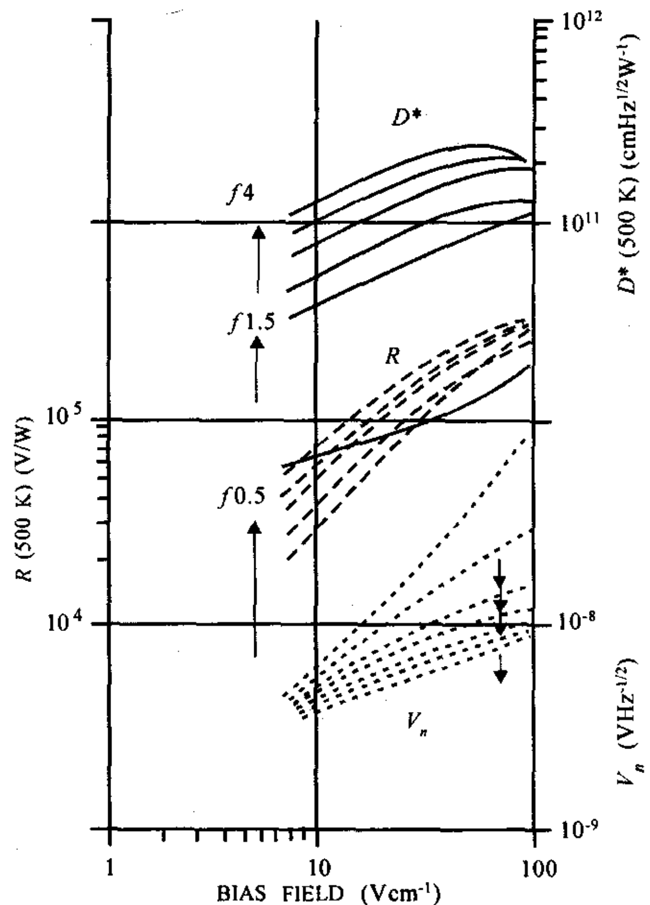

Figure 23. Variation of the performance of a SPRITE detector with bias field and field of view: λ_c =11 µm, T = 77 K.

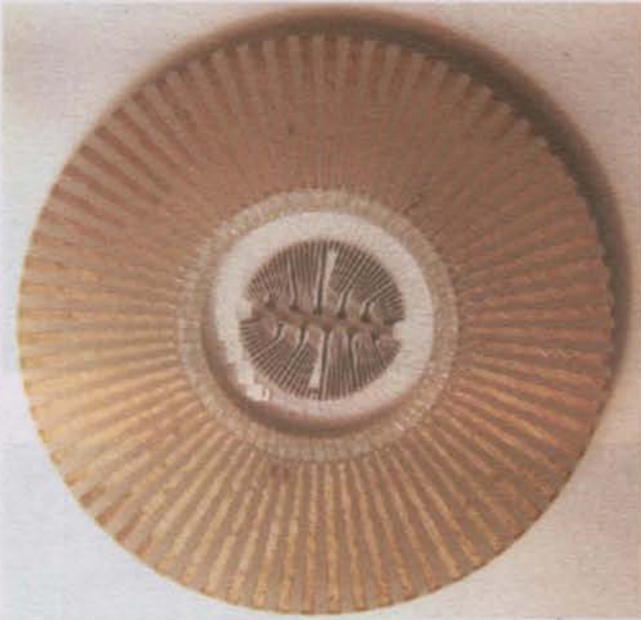

Figure 24(a). A 60-element photoconductive array on a PCB

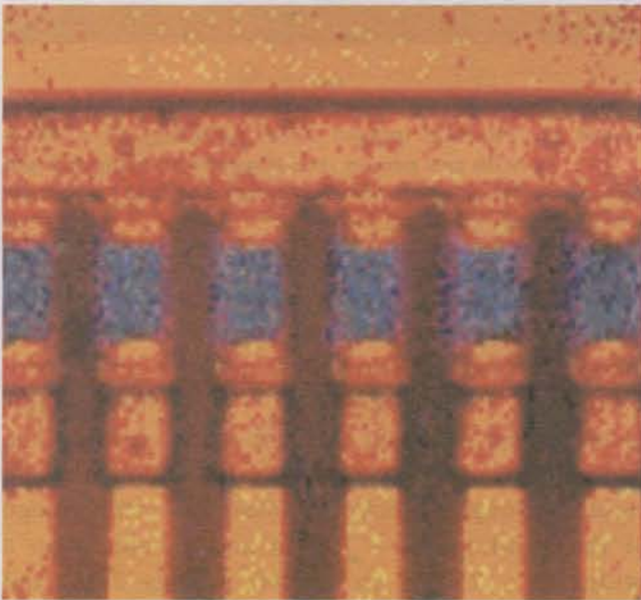

Figure 24(b). Partial view of a few detector elements of a 60-element photoconductive array.

The detectivity increases with bias field as $E^{1/2}$ and also increases with the reduction in FOV. Responsivity shows approximate linear dependence and noise square root dependence on bias field. In the wide FOV ($f\# < 1$), the detectivity and responsivity values are anomalously low. Davis[74] studied the adverse effect of high signal photon fluxes on the

Figure 24(c). A 60- element photoconuctive array as a packaged device.

responsivity. Ashley[66], *et al.* optimised readout geometry and shape of the elements to overcome background effects, improving the spatial resolution in these detectors. Subsequently, several workers carried out further work on improving the performance of SPRITE detectors and their use in system design and implementation[69,72,73,137,138].

A review on the development of photoconductive linear arrays for thermal imaging at this laboratory was reported recently by Singh[114]. The arrays were fabricated using $n\text{-}Hg_{1-x}Cd_xTe$ with $x = 0.214 \pm 0.003$, carrier concentration, $n_0 \leq 4 \times 10^{14}$ cm^{-3}, mobility, $\mu_e \sim 1\text{-}2 \times 10^5$ cm^2/V.s and minority carrier lifetime, $\tau \geq 1 \mu$s. Lifetime measurements using photoconductive decay and microwave reflection techniques served both as diagnostic and process-monitoring tools at different stages of device fabrication, i.e., stages of lapping and polishing during sample preparation, after wafer passivation, and finally on the completed devices. Process-induced material damage in the MCT has been estimated using lifetime measurement[116]. A 60-element array mounted on a PCB along with magnified partial view of few elements and a device-dewar package are shown in Fig. 24 (a-c). A yield of 27 per cent with arrays R_v in the range $1\text{-}10 \times 10^4$ V/W and, D^*_{BB} in the range

1-4 × 10^{10} cmHz$^{1/2}$/W at 80 K using 34° FOV has been achieved. BLIP-dominated performance was attained in several arrays[136]. The relative spectral responsivity of an element in an array with peak wavelength at 11.0 μm and cutoff at 12.7 μm is shown[139] in Fig. 25.

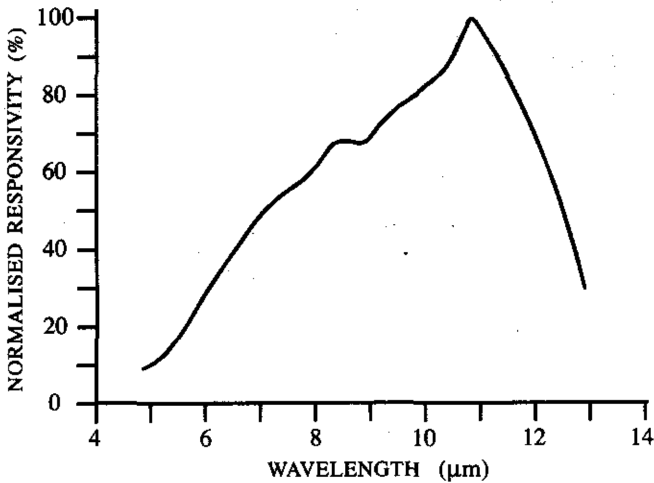

Figure 25. Relative spectral response of a photoconductive $Hg_{1-x}Cd_xTe$ (x = 0.1 eV) detector =11.0 μm and λ_{cutoff} = 12.7 μm.

The peak spectral detectivity of the element is 7.6 × 10^{10} cmHz$^{1/2}$/W. A typical noise density spectrum of an element is shown in Fig. 26 having a corner frequency f_c ~ 540 Hz and frequency-independent noise density of ~ 6.5 nV/Hz$^{1/2}$.

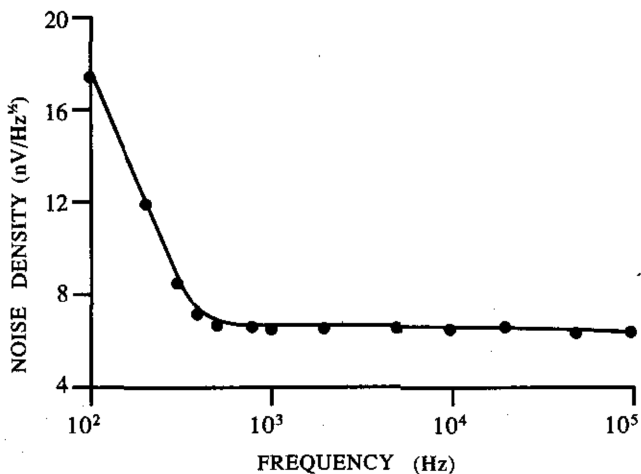

Figure 26. Typical noise density spectrum of an element of a photoconductive detector having a corner frequency f_c ~ 540 Hz and frequency-independent noise density of ~ 6.5 nV/Hz$^{1/2}$.

(a)

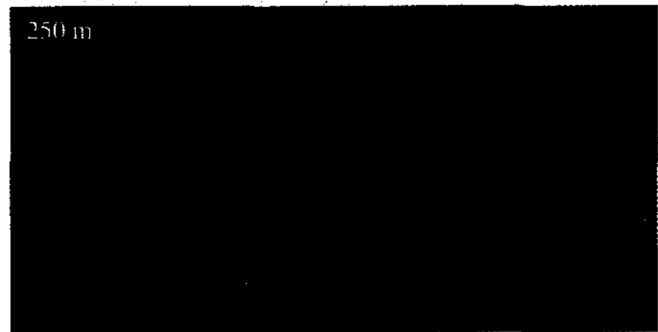

(b)

***Figure 27.* Thermal images of (a) buildings at ~ 700 m with two persons standing shown encircled and the trees in the foreground and (b) a vehicle at ~ 250 m.**

The 1/*f* noise corner frequency f_c as low as 50 Hz has been obtained for some devices[140]. Thermal imaging was done using these detector arrays with average D^* ~ 1 × 10^{10} cmHz$^{1/2}$/W. Several targets in the range of about 2-3 km were viewed. The two microwave towers at ~ 2 km could also be sighted through a blanket of smog. A thermal image of the buildings at ~ 700 m and a vehicle on a bridge at ~ 250 m are shown in Figs 27(a) and 27(b), respectively.

7. SUMMARY

After presenting a brief account of the historic perspective of the IR photon detectors, the relative merits and demerits of the scanning versus staring thermal imaging systems have been brought out and the need for further refinement on the subject of photoconductive detector design and processing technology has been emphasised. Subsequently, impor-

tant performance parameters of the photoconductive detectors in standard as well as SPRITE configurations and the often used basic formulations have been described. The key issues of detector design have been critically examined. The detector processing sequence is then presented in the form of a summary flow chart. Some of the critical processing steps have been dealt in sufficient detail. Finally, a few selective illustrations of photoconductive detector technology have been presented.

ACKNOWLEDGEMENTS

The authors would like to express their gratitude to Dr Vikram Kumar, the then Director SSPL, Delhi, for the permission to publish this paper. Thanks are also due to Dr V. Gopal and Dr R.K. Bhan for their useful discussions and the other members of IR Division for their cooperation.

REFERENCES

1. Keyes, R.J. Introduction. *In* Optical and IR detectors, edited by R.J. Keyes, Ch. 1, pp.1-4. Topics in Applied Physics, (Ed. 2), Vol. **19**. Springer-Verlag, Berlin, 1980.

2. Kruse, P.W. The photon detection process. *In* Optical and IR detectors, edited by R.J. Keyes, Ch. 2, pp.5-69. Topics in Applied Physics, (Ed. 2), Vol. **19**. Springer-Verlag Berlin, 1980.

3. Kruse, P.W.; McGlauchlin, L.D. & McQuistan, R.B. Element of infrared technology: Generation, transmission and detection. Wiley, New York, 1962.

4. Smith, R.A.; Jones, F.E. & Chasmar, R.P. The detection and measurement of infrared radiation, (Ed. 2), Oxford University Press, London, 1968.

5. Hudson, R.D. Introduction to detectors. *In* Infrared system engineering, Ch.7. John Wiley & Sons, New York, 1969.

6. Lloyd, J.M. Thermal imaging systems. Plenum Press, New York, 1975.

7. Hudson, R.D. & Hudson, J.W. Infrared detectors. Dowden, Hutchinson and Ross, Stroudsburg, 1975.

8. Keyes, R.J.(Ed.) Optical and IR detectors. Topics in Applied Physics, Ed. 2, Vol. **19**, Springer-Verlag, Berlin, 1980.

9. Elliott, C.T. Infrared detectors. *In* Handbook on semiconductors, edited by T.S. Moss, Vol. **4**, edited by C. Hilsum, 1981. (Also See Ed. 2, 1993).

10. Elliott, C.T. Photoconductive detectors in *HgCdTe*. *In* Properties of narrow gap cadmium-based compounds, edited by P. Capper. INSPEC, EMIS Datareviews, IEE, London, 1994. pp. 311-22.

11. Dereniak, E.L. & Crowe, D.G. Optical radiation detectors. John Wiley, New York, 1984.

12. Knowles, P. Mercury cadmium telluride detectors for thermal imaging. *GEC J. Research*, 1984, **2**, 141-56.

13. Vincent, J.D. Fundamentals of infrared detector operation and testing. Ch. 4 and 5. Wiley, New York, 1989.

14. Wolfe, W.L. & Zissis G.L. (Eds.). The infrared handbook. IRIA Series in Infrared and Electro Optics. Optical Engineering Press, Bellingham, WA, 1993.

15. Rogalski, A. New ternary alloy systems for infrared detectors. *In* SPIE Optical Engineering Press, Bellingham, WA, 1994.

16. Rogalski, A. Infrared photon detectors. SPIE Optical Engineering Press, Bellingham, WA, 1995.

17. Schlessinger, M. Infrared technology: Fundamentals. Marcel Dekkers, 1995.

18. Wolfe, W.L. Introduction to infrared system design. SPIE Optical Engineering Press, Bellingham, WA, 1996.

19. Dereniak, E.L. & Boreman, G.D. Infrared detectors and systems. John Wiley, New York, 1996.

20. Driggers, R.J.; Cox, P. & Edwards, T. Introduction to infrared and electro-optical system. Artech House, London, 1999.

21. Strzempke, T. & Pritchard, D. Surveillance applications of infrared imaging. *Photonics Spectra,* 1990, **24**, 127-32.

22. Rittner, E.S. Electron processes in photoconductors. *In* Photoconductivity Conference, edited by R. Breckenbridge, B. Russel and E. Hahn, Atlantic City, 1954. Wiley, New York, 1956. pp.215-68.

23. Long, D. & Schmit, J.L. Mercury-cadmium telluride and closely related alloys. *In* Semiconductors and semimetals, edited by R. K. Willardson and A.C. Beer, Vol. 5. Academic Press, New York, 1970. pp. 175-255.

24. Long, D. Photovoltaic and photoconductive infrared detectors. *In* Optical and IR detectors, edited by R.J. Keyes, Ch. 4. pp.101-47. Topics in Applied Physics, Vol. **19**. Springer-Verlag, Berlin, 1980.

25. Kruse, P.W. The emergence of $Hg_{1-x}Cd_xTe$ as a modern infrared sensitive material. *In* Semiconductors and semimetals, edited by R. K. Willardson and A.C. Beer. Vol. **18**. Academic Press, New York, 1981. pp. 1-20.

26. Rogalski, A. & Piotrowski, J. Intrinsic infrared detectors. *Prog. Quant. Electro.,* 1988, **12**, 87-289.

27 Rogalski, A. New trends in semiconductor infrared detectors. *Optical Engineering,* 1994, **33**, 1395-412.

28. Smith, W. Effect of light on selenium during the passage of an electric current. *Nature,* 1873, **7**, 303.

29. Bose, J.C. Detectors for electrical disturbances. U.S. Patent No USP-755840, 1904.

30. Case, T.W. Notes on the change of resistance of certain substances in light. *Physics Review,* 1917, **9**, 305-10.

31. Kutzscher, E.W. Review on detectors of infrared radiation. *Electro-Opt. Syst. Design,* 1973, **5**, 30.

32. Hudson, R.D. & Hudson, J.W. Infrared detectors. Ch. 7. Dowden, Hutchinson and Ross, Stroudsburg, 1975. pp. 264-303.

33. Kushman, R.J. Film-type infrared photoconductors. *Proceedings IRE,* 1959, **47,** 1471-75.

34. Levine, B.F. Quantum-well infrared photodetectors. *J. Appl. Phys.,* 1993, **74,** R1-R81.

35. Lawson, W.D.; Nielson, S.; Putley, E.H. & Young, A.S. Preperation and properties of *HgTe* and mixed crystals of *HgTe-CdTe. J. Phys. Chem. Solids,* 1959, **9,** 325-29.

36. Charlton, D.E. Recent developments in *HgCdTe* infrared detectors. *J. Crystal Growth,* 1982, **59**, 98-110.

37. Sarusi, G.; Levine, B.F.; Pearson, S.J.; Bandara, K.M.S. & Leibenguth, R.E. Improved performance of quantum-well infrared photodetectors using random scattering optical coupling. *Appl. Phys. Lett.,* 1994, **64**, 960-62.

38. Gunapala, S.D. & Bandara, S.V. Quantum-well photodetector (QWIP) FPAs. *Appl. Phys. Lett.,* 1994, **64**, 197-78.

39. Liu, H.C. Quantum-well infrared photodetector physics and novel devices. Intersubband transitions in quantum-well. Ch. 3. *In* Semiconductors and semimetals, Vol. **62** edited by H. C. Liu and F. Capasso. Academic Press, 2000. pp. 129-93.

40. Borrello, S. & Levinstein, H. Preperation and properties of mercury-doped germanium detectors. *J. Appl. Phys.,* 1962, **33**, 2947-950.

41. Kruse, P.W. & Skatrud, D.D. Uncooled infrared imaging arrays and systems. *In* Semiconductors and semimetals, Vol. **47**, edited by R.K. Willardson and E.R. Weber. Academic Press, New York, 1997.

42. Tennent, W.E.; Cabelli, S. & Spariosu, K. Prospects of uncooled *HgCdTe* detector technology. *J. Electro. Mater.*, 1999, **28**, 582-88.

43. Elliott, C.T.; Day, D. & Wilson, D.J. An integrating detector for serial scan thermal imaging. *Infrared Physics*, 1982, **22**, 31-42.

44. Blackburn, A.; Blackman, M.V.; Charlton, D.E.; Dunn, W.A.E.; Jenner, M.D.; Oliver, K.J. & Wotherspoon, J.T.M. The practical realisation and performance of SPRITE detectors. *Infrared Physics*, 1982, **22**, 57-64.

45. Reine, M.B. & Broudy, R.M. A review of *HgCdTe* infrared detector technology. *SPIE Proceedings*, 1977, **124**, 80-89.

46. Broudy, R.M. & Mazurczyk, V.J. $Hg_{1-x}Cd_xTe$ photoconductors. *In* Semiconductors and semimetals, Vol. **18**, edited by R. K. Willardson & A.C. Beer. Academic Press, New York, 1981. pp. 157-99.

47. Reine, M.B. Status of *HgCdTe* detector technology. *Proceedings SPIE*, 1983, **443**, 2-10.

48. Reine, M.B.; Maschhoff, K.R.; Tobin, S.P.; Norton, P.W.; Mroczkowski, J.A. & Krueger, E.E. The impact of characterisation techniques on *HgCdTe* infrared detector technology. *Semicond. Sci. Technol.*, 1993, **8**, 788-04.

49. Capper, P. Narrow-gap II-VI compounds for optoelectronic and electromagnetic applications. *In* Chapman and Hall, London, 1997. pp. 433-49.

50. Smith, D.L. Theory of generation-recombination noise and responsivity in overlap structure photoconductors. *J. Appl. Phys.*, 1983, **54**, 5441-448.

51. Smith, D.L. Effect of blocking contacts on generation-recombination noise and responsivity in intrinsic photoconductors. *J. Appl. Phys.*, 1984, **56**, 1663-669.

52. Jozwikowska, A.; Jozwikowski, K. & Rogalski, A. Performance of mercury cadmium telluride photoconductive detectors. *Infrared Physics*, 1991, **31**, 543-54.

53. Bicknell, W.E. Space charge solution of Rittner photoconductor equation for a *HgCdTe* detector. *Infrared Phys. & Technol.*, 2002, **43**, 39-50.

54. Kolodny & Kidron, I. Two-dimensional effects in intrinsic photoconductive detectors. *Infrared Physics*, 1982, **22**, 9-22.

55. Musca, C.A.; Siliquini, J.F.; Fynn, K.A.; Nener, B.D.; Farone, L. & Irvine, S.J.C. MOCVD grown wider bandgap capping layers in *HgCdTe* long wavelength infrared photoconductors. *Semicond. Sci. Technol.*, 1996, **11**, 1912-19.

56. Smith, E.P.G.; Musca, C.A. & Farone, L. Two-dimensional modelling of *HgCdTe* photoconductive detectors. *Infrared Phys. & Technol.*, 2000, **41**, 175-86.

57. Gopal, V. Relative performance of a photoconductive detector in constant current and constant voltage bias modes. *Infrared Physics*, 1981, **21**, 31-36.

58. Dhar, V. Quantum efficiency. Marcel and Dekker Encyclopedia of Optical Engineering, edited by R.G. Driggers, 2002.

59. Igras, E.; Piotrowski, J. & Piotrowski, T. Ultimate detectivity of *CdHgTe* infrared photoconductors. *Infrared Physics*, 1979, **19**, 143-49.

60. Eppeldauer, G.P. & Martin, R. J. Photocurrent measurement of PC and PV *HgCdTe* detectors. *J. Res. Natl. Stand. Technol.*, 2001, **106**, 577-87.

61. Norton, P.R. Infrared detectors in the next millennium. SPIE Conference on Infrared Technology and Applications, XXV, Orlando, Florida. Vol. **3698**, April 1999. pp. 652-65.

62. Kinch, M.A.; Borello, S.R. & Simmons, A. 0.1 eV *HgCdTe* photoconductive detector performance. *Infrared Physics,* 1977, **17**, 127-35.

63. Elliott, C.T. New detectors for thermal imaging systems. *Electronic Letters,* 1981, **17**, 312-13.

64. Chairi, J.A. & Morten, F.D. Detectors for thermal imaging. *Electro. Components Appl.,* 1982, **4**, 242-53.

65. Elliott, C.T. Infrared detectors with integrated signal processing. *In* Solid state devices, edited by A. Goetzberger and M. Zerbst. Verlag Chemie, Weinheim, 1983. pp.175-201.

66. Ashley, T.; Elliott, C.T.; White, A.M.; Wotherspoon, J.T.M. & Johns, M.D. Optimisation of spatial resolution in SPRITE detectors. *Infrared Physics,* 1984, **24**, 25-33.

67. Wotherspoon, J.T.M.; Dean, R.J. & Johns, M.D. Developments in SPRITE detectors. *Proceedings SPIE,* 1984, **510**, 102-12.

68. Campbell, A.; Elliott, C.T. & White, A.M. Optimisation of SPRITE detectors in anamorphic imaging systems. *Infrared Physics*, 1987, **27**, 125-33.

69. Dean, A.B.; Dennis, P.N.J.; Elliott, C.T.; Hibbert, D. & Wotherspoon, J.T.M. The serial addition of SPRITE infrared detectors. *Infrared Physics,* 1988, **28**, 271-78.

70. Dyson, C.M. Thermal-radiation imaging devices and systems. U.K. Patent Application No UKP–2,199,986 A, 1988.

71. Elliott, C.T. SPRITE detectors and staring arrays in $Hg_{1-x}Cd_xTe$. *Proceedings SPIE,* 1988, **1038**, 2-8.

72. Braim, S.P.; Foord, A. & Thomas, M.W. System implementation of a serial array of SPRITE infrared detectors. *Infrared Physics,* 1989, **29**, 907-14.

73. Severn, J.; Hibbert, D.A.; Mistry, R.; Elliott C.T. & Davis, A.P. The design and performance options for SPRITE detectors and staring arrays. *In* Fourth International Conference on Advanced Infrared Detectors and Systems. IEE, London, 1990. pp. 9-14.

74. Davis, A.P. Effect of high signal photon fluxes on the responsivity of SPRITE detectors. *Infrared Physics,* 1992, **33**, 301-05.

75. Williams, R.L. Sensitivity limits of 0.1 eV intrinsic photoconductors. *Infrared Physics,* 1968, **8**, 337-43.

76. Johnson, M.R. Sweep-out effects in $Hg_{1-x}Cd_xTe$ photoconductors. *J. Appl. Phys.,* 1972, **43**, 3090-093.

77. Emmons, S.P. & Ashley, K.L. Minority-carrier sweep-out in 0.09 eV *HgCdTe. Appl. Phys. Lett.,* 1972, **20**, 241-42.

78. Kinch, M.A. & Borello, S.R. 0.1 eV *HgCdTe* photodetectors. *Infrared Physics,* 1975, **15**, 11-24.

79. Kinch, M.A.; Borello, S.R.; Breazeale, D.H. & Simmons, A. Geometrical enhancement of *HgCdTe* photoconductive detectors. *Infrared Physics,* 1977, **17**, 137-45.

80. White, A. M. Recombination in a graded n-n+ contact region in a narrow-gap semiconductor. *Journal of Physics, C: Solidstate Physics,* 1984, **17**, 4889-896.

81. Kumar, R.; Gupta, S.; Gopal, V. & Chhabra, K.C. Dependence of responsivity on the structure of a blocking contact in an intrinsic *HgCdTe* photoconductor. *Infrared Physics,* 1991, **31**, 101-07.

82. Gopal, V.; Kumar, R. & Chhabra, K.C. A n^{2+}-n^{+}-n blocking contact structure for an intrinsic photoconductor. *Infrared Physics,* 1991, **31**, 435-40.

83. Smith, D.L.; Arch, D.K.; Wood, R.A. & Scott, M.W. *HgCdTe* heterojunction contact photoconductor. *Appl. Phys. Lett.*, 1984, **45**, 83-85.

84. Arch, D.K.; Wood, R.A. & Smith, D.L. High responsivity *HgCdTe* heterojunction photoconductor. *J. Appl. Phys.*, 1985, **58**, 2360-365.

85. Musca, C.A. & Siliquini, J.F. Heterojunction blocking contacts in MOCVD grown $Hg_{1-x}Cd_xTe$ long wavelength infrared photoconductors. *IEEE Trans. Electron. Devices*, 1997, **44**, 239-49.

86. Margalit, S. & Nemirovsky, Y. Diffusion of Indium in $Hg_{1-x}Cd_xTe$. *J. Electrchem. Soc.: Solidstate Sci. Technol.*, 1980, **127**, 1406-408.

87. O'Dette, P.; Tarnowski, G.; Lukach, V.; Krueger, M. & Lovecchio, P. Optimisation of dry etch process conditions for *HgCdTe* arrays. *J. Electron. Mater.*, 1999, **28**, 821-25.

88. Blackman, M. V.; Charlton, D.E.; Jenner, M.D.; Purdy, D.R.; Wotherspoon, J.T.M.; Elliott C.T. & White, A.M. Type conversion in *HgCdTe* by ion beam treatment. *Electronics Letters,* 1987, **23**, 978-79.

89. Shacham-Diamond, Y.J. & Kidron, I. Contact and bulk effects in intrinsic photoconductive infrared detectors. *Infrared Physics*, 1981, **21**, 105-15.

90. Bahir, G. & Finkman, E. Ion beam milling effect on electrical properties of $Hg_{1-x}Cd_xTe$. *J. Vac. Sci. Technol.*, 1989, **A 7**, 348-53.

91. Brogowski, P.; Mucha, H. & Piotrowski, J. Modification of mercury cadmium telluride, mercury manganese telluride and mercury zinc telluride by ion etching. *Phys. Stat. Sol.*, 1989, **114(a)**, K37-K40.

92. Brogowski, P.;S Rutkowski, J.; Piotrowski, J. & Mucha, H. Ion beam milling effect on surface properties of *HgCdTe*. *Electron Technology,* 1991, **24**, 93-96.

93. Elkind, J.L. Ion mill damage in *n-HgCdTe*. *J. Vac. Sci. Technol.*, 1992, **B10**, 1460-465.

94. Baker, I.M. & Maxey, C.D. Summary of *HgCdTe* 2-D array technology in UK. *J. Electr. Mater.,* 2001, **30**, 682-89.

95. Mittal, V.; Gupta, I.; Sharma, R.K.; Singh, R.; Arora, S.C.; Singh, K.P.; Singh, B.V. & Gopal, V. Study of ion beam milling effect on some electrical properties of *HgCdTe*. Proceedings IX–IWPSD–2001, edited by V. Kumar and P.K. Basu. Narosa, New Delhi, 2001. pp. 1125-128.

96. Baron, R.; Shifrin, G.A.; Marsh, O.J. & Mayer, J.W. Electrical behaviour of group III and V implanted dopants in silicon. *J. Appl. Phys.*, 1969, **40**, 3702-719.

97. Dearnaley, G.; Freeman, J.H.; Nelson, R.S. & Stephen, J. Ion implantation, North Holland Publishers, Amsterdam, 1973.

98. Ashley, T. & Elliott, C.T. Accumulation effects at contacts to *n*-type cadmium-mercury-telluride photoconductors. *Infrared Physics*, 1982, **22**, 367-76.

99. Musca, C.A.; Siliquini, J.F.; Nener, B.D. & Farone, L. Passivation and surface effects in long wavelength infrared *HgCdTe* photoconductors. *SPIE*, 1995, **2552**, 158-69.

100. Pal, R.; Bhan, R. K.; Chhabra, K.C. & Agnihotri, O.P. Analysis of the effect of surface passivant charges on *HgCdTe* photoconductive detectors. *Semicond. Sci. Technol.*, 1996, **11**, 231-37.

101 Ashokan, R.; Gandhi, A.; Bharat Veer; Sharma, B.L.; Dhar, V.; Srivastava, S.; Makani, S.; Dewan, H.S. & Gopal, V. Contact resistance studies on indium/*n*- $Hg_{1-x}Cd_xTe$. *In* Proceedings IX–IWPSD–1997, edited by V. Kumar and S.K. Aggarwal. Narosa, New Delhi, 1998. pp. 774-77.

102. Pal, R.; Gopal, V. & Kumar, V. Evaluation of processing-induced variations in a mercury cadmium telluride photoconductive (PC) array. *Infrared Phys. & Technol.*, 1998, **39**, 315-21.

103. Nemirovsky, Y. & Bahir, G. Passivation of mercury cadmium telluride surfaces. *J. Vac. Sci. Technol.*, 1989, **A7**, 450-59.

104. Nemirovsky, Y. Passivation with II-VI compounds. *J. Vac. Sci. Technol.*, 1990, **A8**, 1185-187.

105. Singh, R.; Gupta, A.K. & Chhabra, K.C. Surface passivation of mercury-cadmium-telluride infrared detectors. *Def. Sci. J.*, 1991, **41**, 205-39.

106. Bahir, G.; Ariel, V.; Garber, V.; Rosenfeld, D. & Sher, A. Electrical properties of epitaxially grown *CdTe* passivation for long wavelength *HgCdTe* photodiodes. *Appl. Phys. Lett.*, 1994, **65**, 2725-727.

107. Bubulac, L.O.; Tenant, W. E.; Bajaj, J.; Sheng, J.; Brigham, R.; Vanderwyck, A.H.B.; Zandian, M. & Mc Levige, W.V. Characterisation of *CdTe* for *HgCdTe* surface passivation. *J. Electron. Mater.*, 1995, **24**, 1175-182.

108. Agnihotri, O.P. & Musca, C.A. *Semicond. Sci. Technol.*, 1998, **13**, 839.

109. Pal, R. Studies on passivation of *HgCdTe*. Indian Institute of Technology Delhi, New Delhi, 2000. PhD Thesis.

110. Pal, R.; Sharma, B.L.; Gopal, V.; Kumar, V. & Agnihotri, O.P. Effect of *HgCdTe*-passivant interface properties on the performance of photoconductive detectors. *Infrared Phys. Technol.*, 1999, **40**, 101-07.

111. Kinch, M.A. Electronic properties of *HgCdTe*. *J. Vac. Sci. Technol.*, 1982, **21**, 215-19.

112. Kinch, M.A. Metal-insulator-semiconductor infrared detectors. *In* Semiconductors and semimetals, edited by R. K. Willardson and A.C. Beer. Vol. **18**, Ch. 7. Academic Press, New York, 1981. pp. 313-84.

113. Bhan, R.K.; Gopal, B. & Saxena, R.S. Effect of fixed charges due to passivant on the performance of *HgCdTe* overlap structure. *Semicond. Sci. Technol.*, 2002, **17**, 590-98.

114. Risal Singh. Development of MCT PC linear arrays for thermal imaging. *In* DRDO Science Spectrum 2002–A Compendium of National Science Day Orations, edited by Dr Mohinder Singh, 2002. pp.217-36.

115. Siliquini, J.F.; Fynn, K.A.; Nener, B.D.; Farone, L. & Hartley, R.H. Improved device technology for epitaxial $Hg_{1-x}Cd_xTe$ infrared photoconductor arrays. *Semicond. Sci. Technol.*, 1994, **9**, 1515-522.

116. Sharma, B.L.; Bedi, P.K.; Arora, S.C.; Sreeniwas; Chaudhury, P.K.; Pal, R.; Gupta, A.K.; Singh, R.; Basu, P.K. & Gopal, V. $Hg_{1-x}Cd_xTe$ LWIR photoconductive linear array fabrication process control through lifetime monitoring. Proceedings X–IWPSD–1999, Vol. 1, edited by V. Kumar and S.K. Agarwal. Allied Publications, New Delhi, 2000. pp. 97-100.

117. Byer, N.E.; Davis, G.D.; Buckner S.P. & Ahearn, J.S. Insulator interfaces with $Hg_{1-x}Cd_xTe$. *In* Insulating films on semiconductors, edited by J.F. Verweij and D.R. Wolters. 1983. pp.238-43.

118. Rhiger, D. R. Use of ellipsometry to characterise the surface of *HgCdTe*. *J. Electron. Mater.*, 1993, **22**, 887-98.

119. Catagnus, P.C. & Baker, C.T. Passivation of mercury cadmium telluride semiconductor surfaces by anodic oxidation.US Patent No USP-3,977,018, 1976.

120. Nemirovsky, Y & Finkman, E. Anodic oxide films on $Hg_{1-x}Cd_xTe$. *J. Electrochem. Soc.*, 1979, **126**, 768-70.

121. Janousek, B.K. & Carscallen, R.C. The mechanism of *(HgCd)Te* oxidation. *J. Appl. Phys.*, 1982, **53**, 1720-726.

122. Chavada, F.R.; Tewari, G. & Gupta, S.C. *Bull. Mater. Sci.*, 1987, **9**, 219.

123. Yadav, R.D.S. & Warrier, A.V.R. Anodic polarisation of *HgTe, CdTe* and $Hg_{1-x}Cd_xTe$ –oxide formation kinetics and omposition. *J. Mater. Sci.*, 1991, **26**, 423-28.

124. Singh, R.; Sharma, B.L.; Mittal, V.; Pathak, H.T.; Srivastava, S.; Pal, R.; Singh, J.P.; Dewan, H.S.; Madaria, R.K.; Basu, P.K. & Warrier, A.V.R. Asymmetric overlap and locking contacts for linear arrays. National Conference on Recent Advances in Conductors (NCRAS), IIT Delhi,1995.

125. Gauthier, A. Process for passivation of photoconductive detectors made of *HgCdTe*. US Patent No. USP - 4,624,715, 1986.

126. Wilson, J.A.; Cotton, V.A.; Silberman, J.; Laser, D.; Spicer, W.E. & Morgen, P. *(HgCd) Te-* SiO_2, interface structures. *J. Vac. Sci. Technol.*,1983, **A1**, 1719-722.

127. Mittal, V.; Monga, K.; Pathak, H.T.; Singh, R.; Gopal, V. & Kumar, V. Some critical processes in the fabrication of PC linear array. *In* Proceedings IX–IWPSD–1997, edited by V. Kumar and S.K. Aggarwal. Narosa, New Delhi, 1998. pp. 803-05.

128. Mittal, V.; Singh, K.P.; Singh, R. & Gopal, V. A study of UV treatment of photoresist for dry processing. *In* Proceedings IX– IWPSD –1997, edited by V. Kumar and S.K. Aggarwal. Narosa, New Delhi, 1998. pp.1215-217.

129. Bhan, R.K.; Mittal, V.; Rawal, D.S.; Naik, A.A.; Sehgal, B.K.; Singh, K.P.; Singh, B.V.; Aneja, B.R.; Sharma, B.L.; Singh, R. & Gopal, V. Effect of ion beam milling on lips prior to lift-off process. *In* Proceedings IX–IWPSD–2001, edited by V. Kumar and P.K. Basu. Narosa , New Delhi, 2001. pp.1049-052.

130. Pathak, H.T.; Gandhi, A.; Khurana, K.; Sharma, A. & Singh, K.P. PLG metal lift-off process for MCT 20–element PC array. *In* National Seminar on IR Devices and their Defence Applications. Delhi, India, 1989. pp.19.1-19.2.

131. Gupta, S.; Mittal, V. & Chhabra, K.C. A clean method for growing uniform 4 µm thick In bumps. *In* Proceedings of the Conference on Physics and Technology of Semiconductor Devices. Pilani, India, 1992.

132. Limperis, T. & Mudar, J. Detectors. Ch. 11. *In* The infrared handbook. IRIA Series in Infrared and Electro Optics. Optical Engineering Press, Bellingham, WA, 1993.

133. Eisenman, W.L.; Merriam, J.D. & Potter, R.F. Operational characteristics of infrared photodetectors. *In* Semiconductors and semimetals, edited by R.K. Willardson and A.C. Beer. Vol. **12**, 1977. pp.1-38.

134. Paugh, R.L. Improving the performance of military IR systems with cryogenic cooling. *Photonic Spectra*, 1994, **28**, 93-95.

135. Borrello, S.R.; Kinch, M. & Lamont, D. Photoconductive *HgCdTe* detector performance with background variations. *Infrared Physics*, 1977, **17**, 121-25.

136. Singh, R.; Sharma, B.L.; Mittal, V.; Pathak, H.T.; Srivastava, S.; Pal, R.; Singh, J.P.; Dewan, H.S.; Madaria, R.K.; Basu, P.K. & Warrier, A.V.R. Asymmetric overlap structures for 0.1 eV MCT PC linear arrays. *In* Proceedings of the VIII International Workshop on Physics of Semiconductor Devices, (IWPSD-1995), edited by K. Lal. Narosa, India, 1996. pp. 208-10.

137. Yamagata, T.; Oda, N.; Miyamoto, K. & Fujino, Y. Size optimisation in SPRITE detector. *In* Proceedings of the Sixth Sensor Symposium, 1986. pp.305-08.

138. Zhijun, X. & Wenqing, F. Optimisation of SPRITE detectors. *Infrared Physics*, 1990, **30**, 489-97.

139. Singh, R.; Sharma, B.L.; Mittal, V.; Pathak, H.T.; Srivastava, S.; Pal, R.; Singh, J.P.;

Dewan, H.S.; Madaria, R.K.; Basu, P.K. & Warrier, A.V.R. Fabrication of *(HgCd)Te* photoconductive linear arrays for thermal imaging in 8-14 μm range. *In* Proceedings of the Emerging Opto-elecctronic Technologies (CEOT). McGraw-Hill, Delhi, 1994. pp. 252-55.

140. Pal, R.; Singh, J.P.; Mittal, V.; Sharma, B.L.; Srivastava, S.; Pathak, H.T.; Singh, R.; Madaria, R.K.; Basu, P.K. & Warrier, A.V.R. Temperature and field-dependence of noise in 0.1 eV MCT PC IR detectors. *In* National Conference on Recent Advancesi n Semiconductors (NCRAS), IIT Delhi, 1995.

Contributors

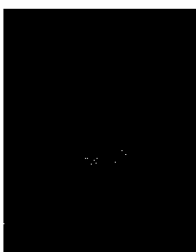

Dr Risal Singh obtained his PhD in Physics from the Indian Institute of Technology (IIT) Delhi, New Delhi, in 1973 and Advanced Diploma in French from the University of Delhi in 1977. Presently, he is working as Sci F at the Solid State Physics Laboratory, (SSPL) Delhi. He was awarded the Alexander von Humboldt (AvH) senior fellowship for pursuing postdoctoral studies at the Institute of Semiconductor Electronics, Faculty of Electrical Engineering, Technical University of Aachen (Germany) during 1981-83. His areas of interest are: MOS device physics and technology, VLSI processing and materials, and infrared detector technology. He has about 50 research publications/ presentations in international journals and conference proceedings. He is a life member of the Materials Research Society of India.

Dr Vandna Mittal obtained her MSc in Physics from the University of Roorkee and received her PhD in thin wear resistant coatings from the IIT Delhi, New Delhi, in 1988. She joined DRDO at the SSPL, Delhi, in 1988 and is presently working as Sci D. Her areas of research are: Infrared detector technology, photolithography, and dry processing technology. She has about 20 research publications/presentations in national/international journals and conference proceedings.